SSRv manuscript No.
(will be inserted by the editor)

The 3D Geometry, 3D Motion, and Hydrodynamics of Oscillating Coronal Loops

Markus J. Aschwanden[1]

Received: 2008-Jan-01 / Accepted: ...

Abstract We transition from two-dimensional (2D) imaging observations of kink-mode loop oscillations in the solar corona to three-dimensional (3D) reconstructions by exploring two new methods: (1) De-projection of 2D loop tracings using the strategy of curvature maximization in 3D space, based on the assumption of force-free magnetic fields; and (2) stereoscopic triangulation of epipolar loop coordinates using coaligned images from the STEREO EUVI/A and B spacecraft. Both methods reveal new features of oscillating loops: non-circularity, non-planarity, and helical geometries. We extend the 3D reconstruction techniques into the time domain and find indications of circularly polarized (torsional) kink-mode oscillations, in contrast to linearly polarized modes assumed previously. We discuss also hydrodynamic effects of coronal loops in non-equilibrium state that are essential for the detection and modeling of kink-mode oscillations.

Keywords Solar corona · Oscillations · Waves

1 Motivation

In this study we focus on the measurement and modeling of the most fundamental physical parameters of coronal loop oscillations, such as the 3D geometry $\mathbf{x}(s)$, the 3D motion $\mathbf{x}(s,t)$, the electron density $n_e(s,t)$, and the electron temperature $T_e(s,t)$, which all can be inferred from EUV or soft X-ray imaging observations only by appropriate geometric modeling. We mostly focus on fast magneto-acoustic waves of the kink-mode type; we do not cover the fast sausage-mode type (since there exist no direct measurements yet) or slow magnetoacoustic waves (which are detected by Doppler shifts and intensity variations rather than by spatial motions). So far, the 3D motion of kink-mode oscillations has not really been addressed in any detail, but was mostly

---

[1]) Solar & Astrophysics Laboratory, Lockheed Martin Advanced Technology Center, Bldg. 252, Org. ADBS, 3251 Hanover St., Palo Alto, CA 94304, USA
Tel.: +650-424-4001
Fax: +650-424-3994
E-mail: aschwanden@lmsal.com

based on amplitude measurements projected into the image plane, while only a few studies attempted to determine the 3D directivity of the oscillatory motion, e.g., the vertical vs. horizontal polarization (direction) of the oscillatory loop motion with respect to the loop plane (Wang & Solanki 2004), or fundamental vs. harmonic amplitude displacements (Van Doorsselaere, Nakariakov, & Verwichte 2007). Since we can only measure 2D coordinates from images, even from stereoscopic spacecraft observations, a proper 3D reconstruction of the loop geometry is a non-trivial task. In addition we have to be aware that also other fundamental physical parameters of oscillating loops, such as the electron density n_e and temperature T_e, require 3D geometric modeling of the loop shape and loop cross-sections.

One of the most desirable goals of coronal seismology is the inference of the coronal magnetic field $\mathbf{B}(\mathbf{x})$, but its determination depends on the loop length (which can only be obtained from the 3D geometry of the loop) and electron densities externally and internally of the oscillating loop,

$$B = \frac{L}{P_{kink}} \sqrt{8\pi\rho_0(1+\rho_e/\rho_0)} \ , \tag{1}$$

where P_{kink} is the kink-mode period, L the full loop length, $\rho_0 = \mu m_p n_e$ the mass density inside the loop, ρ_e the external mass density, m_p the proton mass, and μ the mean molecular weight (e.g., Nakariakov & Ofman 2001, with a different factor in their Eq. 6; Roberts & Nakariakov 2003; Aschwanden 2004).

Moreover, since the kink-mode period also depends somewhat on the geometric curvature, cross-sectional properties, and the gravitational stratification in the loop, accurate determinations require a refined geometry and density modeling. Besides the (asymmetric) fast kink-mode, there exists also a (symmetric) sausage mode, which is manifested by radial density and cross-sectional modulations, which has not been directly measured yet, but requires also geometric and density modeling. In addition, there are a number of other effects that require a careful reconstruction of geometric and physical parameters, such as the detection of other oscillating modes (e.g., torsional modes or propagating waves), asymmetric excitation, the magnetic forces that excite and drive loop oscillations and waves (probably triggered by flares and CMEs), the hydrodynamic physics in oscillating loops, or the physical damping mechanisms that quench the loop oscillations.

A discussion of the data analysis techniques and problems is particularly timely now because new 3D capabilities (from the STEREO mission) and more comprehensive spectroscopic instruments (e.g., Hinode EIS and XRT) have become available that promise new breakthroughs in the field of *coronal seismology*.

2 The 3D Geometry of Oscillating Loops

2.1 Theoretical Treatment of the 3D Loop Geometry

Early theoretical calculations of the dispersion relation of MHD waves treated the solar corona as an unbounded homogeneous medium. Introducing a single magnetic interface (by a mathematical step function) leads to two domains that each can support magneto-acoustic waves, which were called *body waves* (e.g., Roberts 1981a). A new phenomenon that occurs thanks to the presence of a boundary is a wave mode called *surface wave* (Roberts 1981a), e.g., a *shear wave* or *Alfvénic surface wave* in the incompressible fluid limit. The next steps towards a more realistic geometry of coronal loops was the *slender slab* geometry (Roberts 1981b; Edwin & Roberts 1982), and then the *cylindrical flux tube* geometry (Edwin & Roberts 1983), which all are characterized by different values of the density n_e, pressure p, and magnetic field B inside and outside of the flux tube, yielding also different Alfvén speeds v_A and sound speeds c_s inside and outside. In these calculations, the 3D geometry of a coronal loop is thus characterized with a straight cylinder (with a fixed length) and constant cross-section, constant density, constant pressure, and constant magnetic field, which leads to dispersion relations in terms of radial Bessel functions.

The effect of curvature in coronal loops was considered in calculations of the kink-mode period by Van Doorsselaere et al. (2004a), but only small differences in the kink-mode frequency ($\lesssim 12\%$) and damping rate were found, compared with straight cylinders. Also loop curvatures of elliptical shapes were investigated, which sustain particular wave modes and enable wave coupling that modify the damping rate somewhat, but the kink-mode periods are still similar to those of straight cylinders (Diaz 2006).

While most previous theoretical studies dealt with sharp loop boundaries, i.e., a radial step function, the so-called *thin-boundary* layer, alternative studies introduced also *thick-boundary* layers, characterizing the radial cross-sectional density profile $n_e(r)$ with a triangular, Gaussian, or Epstein function. The geometric shape of the loop boundary has a particularly important effect on the damping rate, because the introduced inhomogeneity in density represents a variation of Alfvén speed and thus increases the efficiency of resonant damping and phase mixing (Hollweg 1990; Van Doorsselaere et al. 2004b). The damping of kink modes in curved loops was also investigated for a curved loop with a powerlaw radial density profile, which gives rise to resonant absorption (due to coupling with external Alfvén modes) and wave leakage (by tunneling), but the difference between straight and curved cylinders was again small (Terradas, Oliver, & Ballester 2006).

In summary, theoretical studies have established that the loop curvature and cross-sectional profile have only second-order effects on kink-mode periods calculated from straight cylinders, which therefore are sufficient for coronal seismology and determinations of the coronal magnetic field. However, both loop curvature and inhomogeneous loop cross-section profiles give rise to new surface wave modes, affecting the coupling between different wave modes, and thus have crucial consequences for the damping of different wave modes. Therefore, observational studies of geometric loop parameters might have far-reaching consequences for the diagnostic of coronal wave dissipation and coronal heating.

2.2 Previous Modeling of Loop 3D Geometries

Before we can quantify the 3D motion of oscillating loops, we have first to determine the 3D geometry of a loop at a given instant of time. The simplest method is based on the assumption of a circular 3D geometry (not necessarily semi-circular), which implies that a loop can be fitted in any arbitrary direction with an ellipse, whose major axis corresponds to the circular radius and is oriented perpendicular to the line-of-sight. Such elliptical reconstructions were applied, e.g., to flare loops (Nitta et al. 1999). Additional 3D information can also be obtained from the parallax effect caused by solar rotation (over a day or so), which allows us to infer the 3D geometry of even short-lived active region loops, as long as the embedding magnetic field is quasi-stationary,

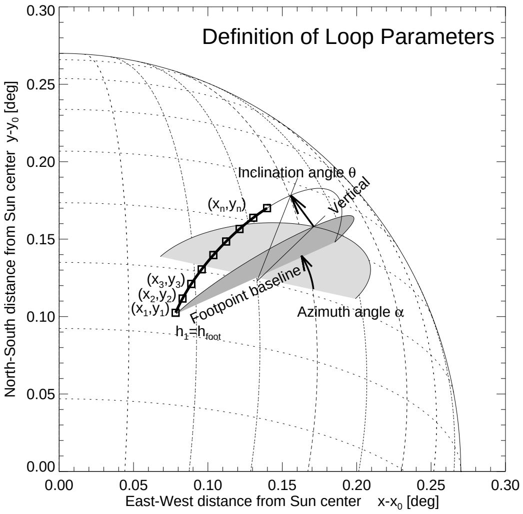

Fig. 1 Definition of loop geometry parameters: loop positions $(x_i, y_i), i = 1, ..., n$, the azimuth angle α between the loop footpoint baseline and heliographic east-west direction, and the inclination angle θ of the loop plane wth respect to the vertical on the solar surface [from Aschwanden et al. 1999a].

a method that was called *dynamic stereoscopy* (Aschwanden et al. 1999a). Alternatively, line-of-sight Doppler velocity measurements of plasma flows along loops have been combined with simple geometric models to infer the true 3D shape of coronal loops, using SUMER and CDS measurements (Alissandrakis et al. 2008). Interestingly, although these methods yield the approximate 3D geometry of a loop, they are not necessarily suitable to track kink-mode oscillations, because the intrinsic geometric shape changes dynamically within a fraction of a kink-mode period and violates the basic assumption of quasi-stationarity used in most 3D reconstruction techniques. However, these methods are useful to infer at least the time-averaged 3D loop geometry, which is sufficient to estimate the approximate loop length L and the average loop inclination angle θ to the vertical (which is important for hydrostatic modeling).

2.3 The Curvature Maximization Method

Since many loops significantly deviate from a circular geometry, we develop here a new method of modeling the 3D geometry of a loop that can be applied to 2D measurements from a single image without making the assumption of circularity and coplanarity.

What we can measure directly from a loop are the 2D coordinates $(x_i, y_i), i = 1, ..., n_i$ at individual loop positions i (Fig. 1). A 3D reconstruction of the loop geometry requires an additional *a priori* assumption that can be used to constrain the third coordinate $(z_i), i = 1, ..., n_i$ along the line-of-sight (LOS). One physically justifyable method is the maximization of the curvature radius in 3D space, because this minimizes the Lorentz force exerted by the magnetic tension force due to the loop curvature (e.g., Priest 1982, p. 102; Aschwanden 2004, p.252),

$$\mathbf{F}_{curv} = (\mathbf{j} \times \mathbf{B})_{curv} = \frac{B^2}{4\pi} \frac{1}{r_{curv}} \mathbf{e}_n \ , \tag{2}$$

where **j** is the current density, r_{curv} is the loop curvature, and $\mathbf{e}_n$ is the vector perpendicular to the loop pointing to the curvature center. The curvature force tries to reduce the curvature in a force-free field until it is balanced by other forces (e.g., the magnetic or thermal pressure). Assuming that other forces along the loop are constant, a circular shape with a constant curvature radius r_{curv} represents the closest solution to a force-free magnetic field, according to Eq. (2). However, the assumption of a strictly circular geometry generally over-constrains the data. A viable strategy is to reconstruct the 3D geometry by de-projecting the 2D coordinates of a traced loop using the rule of maximum curvature radius in 3D space. We will give a practical recipe for this *curvature maximization method* in the following.

A classical kink-mode oscillation event is shown in Fig. 2, observed with TRACE during the 1998-Jul-14, 12:45 UT, flare, analyzed in Aschwanden et al. (1999b) and Nakariakov et al. (1999). The projected 2D geometry is shown in Fig. 2 (bottom left), which can be fitted with a circular segment (i.e., a segment of an ellipse in projection). The elliptical fit can be carried out with no footpoint constraints (requiring 6 free parameters: (l_0, b_0) the heliographic longitude and latitude of the baseline center; h_0 the height of the loop center above the base; l_{base} the baseline distance between the two footpoints; α the azimuth angle of the baseline; and θ the inclination angle of the loop plane (Fig. 1), or more simply with footpoint constraints (leaving 2 free parameters: h_0 and θ). In Fig. 2 (bottom left) we clearly see significant deviations of the observed 2D loop coordinates (x^{loop}, y^{loop}) from the best circular fit (x^{circ}, y^{circ}), which implies that the circular geometry represents an over-constraint and that the loop is neither circular nor coplanar. In order to estimate the LOS coordinate z^{loop} at a given loop position (x^{loop}, y^{loop}), we can associate the corresponding LOS coordinate z^{circ} of the circular model at the corresponding position (x^{circ}, y^{circ}),

$$z_i^{loop}(x_i^{loop}, y_i^{loop}) = z_j^{circ}(x_j^{circ}, y_j^{circ}) \ , \tag{3}$$

where we define the corresponding 2D positions (x, y) by proportional lengths of the projected loop segments. The (2D-projected) length of a segment of the *observed loop* (with loop length coordinate $s_i, i = 1, ..., n_i$) is

$$s_i = \sum_{i'=2}^{i} \sqrt{(x_{i'} - x_{i'-1})^2 + (y_{i'} - y_{i'-1})^2} \ , \tag{4}$$

with an overall length $l_i = s_{n_i}$ for the observed loop. Similarly, the (2D-projected) length of a segment of the *circular loop model* (with loop length coordinate $s_j, j = 1, ..., n_j$) is

$$s_j = \sum_{j'=2}^{j} \sqrt{(x_{j'} - x_{j'-1})^2 + (y_{j'} - y_{j'-1})^2} \ , \tag{5}$$

with an overall length $l_j = s_{n_j}$ for the circular model loop. Since the observed loop and the circular model loop might have slightly different lengths, we simply require proportionality in the normalized (2D-projected) loop lengths,

$$\frac{s_i}{l_i} = \frac{s_j}{l_j} \ . \tag{6}$$

As an example, we display in Fig. 3 the solution of the 3D reconstruction of the same loop as observed in Fig. 2, with de-projections into the orthogonal (x, z) and (y, z)

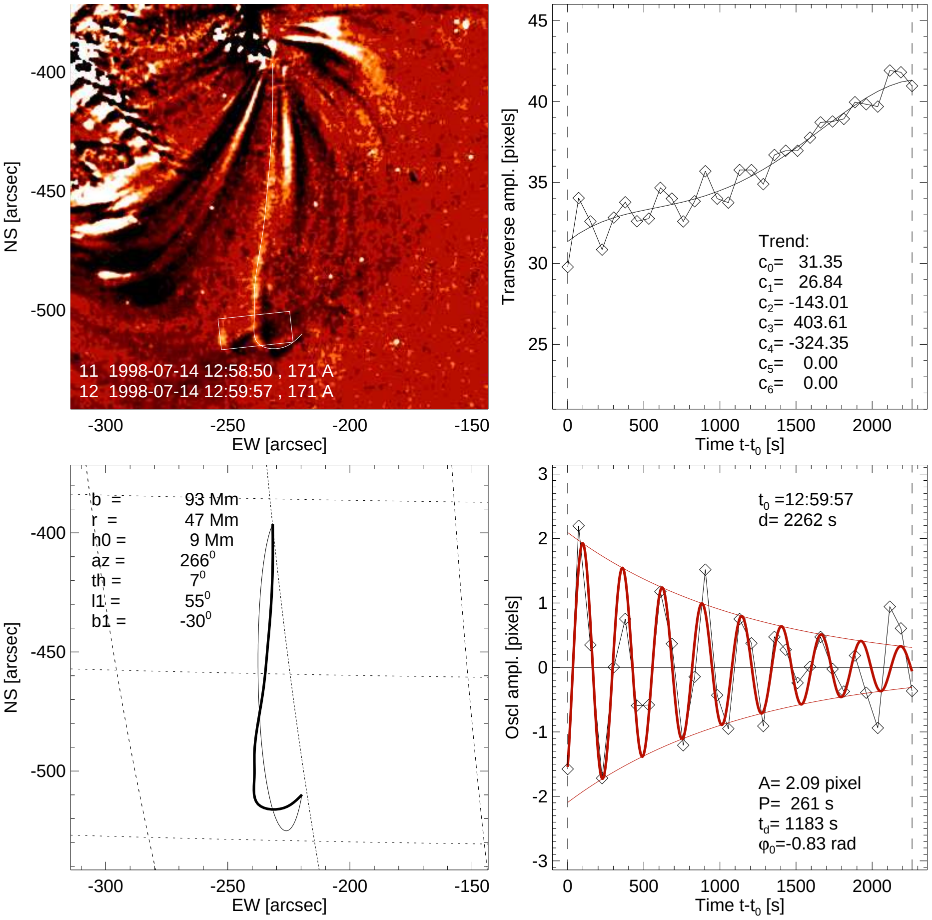

Fig. 2 Oscillation event 1998-Jul-14, 12:45 UT, analyzed by Aschwanden et al. (1999b) and Nakariakov et al. (1999). *Top left:* Difference image with a rectangular box indicating where transverse oscillations are analyzed. *Bottom left:* 3D geometry of observed loop (thick line) fitted with a circular model (thin line), specified by the baseline (b), loop radius (r), height of circular loop center (h_0), azimuth angle of baseline (α), inclination angle of loop plane to vertical (θ), heliographic longitude (l1) and latitude (b1) of baseline midpoint. The spacing of the heliographic grid is 5^0 ($\approx$ 60 Mm). *Top right:* Transverse loop position (in pixel units), where the trend is fitted with a polynomial (with coefficients $c_0, c_1, c_2, c_3, \ldots$). *Bottom right:* Detrended oscillation, fitted with an exponentially decaying oscillatory function (with amplitude A, period P, decay time t_d, phase φ_0). t_0 is the start time (to which the phase φ_0 is referenced), and d is the duration of the fitted interval [from Aschwanden et al. 1999b].

planes. Note that this solution for the 3D geometry has (1) an identical 2D projection as observed, and (2) maximizes the curvature radius in 3D space as close as possible to the circular model (without being inconsistent with the observed 2D projection).

With this 3D reconstruction approach, which we call the *curvature maximization method*, we have a unique solution for the unknown LOS coordinate z_i^{loops} for every loop position (x_i^{loop}, y_i^{loop}) (even for non-circular and non-planar loops), a solution

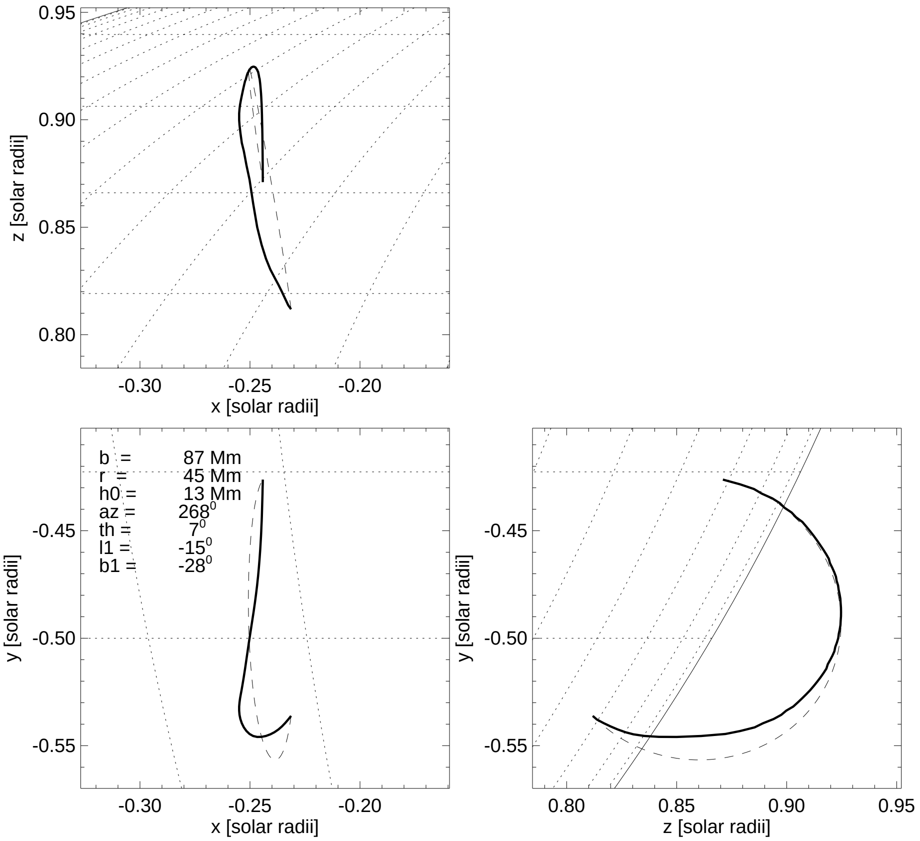

Fig. 3 3D reconstruction of the loop geometry for the oscillating loop shown in Fig. 1, using the method of curvature maximization. The circular model (thin curves) and the reconstructed observed loop (thick curves) are shown in the image or (x,y)-plane (bottom left), and deprojected into the (x,z)-plane (top left) and in the (z,y)-plane, where z is the direction of the observer's line-of-sight (FOV), perpendicular to the image plane.

that is close to the maximum (constant) curvature radius, and thus close to a force-free magnetic field solution. A caveat of this 3D reconstruction method is that the solution is not expected to be realistic in locations of large force gradients (e.g., near current sheets or X-points) or in strong flows (e.g., near streamers, erupting filaments, or CMEs). Nevertheless, this method is fully consistent with the observed 2D projection coordinates and provides a robust estimate of the 3D geometry that can always be obtained from a single image (especially in the absence of stereoscopic data).

2.4 Stereoscopically Observed Oscillating Loops

Since the launch of STEREO in December 2006, stereoscopic data from two identical EUV telescopes are available with spacecraft separation angles of $\alpha_{sep} \lesssim 90^\circ$ during the first two years of the mission (Howard et al. 2008; Wuelser et al. 2004). In

Table 1 Flare and CME events with loop oscillations and waves observed with STEREO/EUVI

#	Date	Time	Heliogr.	Stereo	GOES	RHESSI[1]			EUVI[2]		CME[3]
			location	angle	class	E	P	A	B	Com.	Rep.
		(UT)		(deg)		(keV)	(cts/s)	(10^5	DN/s)		
8	07/01/12	01:00-03:00	N00W87	0.2	C1.5	12	34	31.2	....	IPEW	L
35	07/05/02	23:20-23:59	S09W16	6.3	C8.5	12	30	23.0	17.3	IPW	...
43	07/05/16	17:10-18:10	N03E34	8.2	C2.9	12	26	12.7	9.9	IPDW	LS
46	07/05/19	12:40-13:20	N03W03	8.6	B1.3	12	46	17.4	13.9	IPEDW	LS
100	07/06/08	12:30-13:30	S08W08	11.9	B7.6	12	28	7.9	5.9	IPDW	LS
104	07/06/09	13:20-14:40	S10W23	12.1	M1.0	12	184	69.4	45.8	IW	L
109	07/06/27	17:30-18:30	S20E89	15.4	C1.3	3	34	2.9	2.4	IDOW	...
133	07/08/06	15:20-15:50	S12E38	23.3	C1.1	12	32	7.8	25.2	IPW	LS
175	07/12/31	00:30-01:40	S15E87	44.0	C8.3	25	288	7.5	39.3	IPDOW	LS
183	08/03/25	18:30-19:30	S25E90	47.2	M1.7	12	944	17.8	192.2	IPDEW	LS

#) Event identification number in EUVI flare and CME catalog:
http://secchi.lmsal.com/EUVI/euvi_events.txt

[1] RHESSI:
E = highest detected energy range: 3-6, 6-12, 12-25, 50-100 keV,
P = peak count rate of RHESSI light curve.

[2] EUVI, comments:
A = background-subtracted peak flux detected in EUVI/A,
B = background-subtracted peak flux detected in EUVI/B,
P = Postflare loop emission,
D = Dimming in EUV,
E = Eruptive feature,
O = Occulted (for A if flare position is east, or for B if west),
W = Waves or oscillations.

[3] CME reports:
L = LASCO/SOHO,
S = SECCHI Cor-1 or Cor-2.

a survey of flare and CME events observed with the SECCHI/EUVI telescope during the first two years of the mission, at least 10 events were identified that contain loop oscillations and/or propagating waves (Aschwanden et al. 2009), which we list in Table 1 (Movies and quicklook plots of these oscillation events are also available at *http://secchi.lmsal.com/EUVI/*). This list of events may not be complete, because oscillating loops and propagating waves were mostly identified by visual inspection of EUVI 171 Å movies, rather than by automated detection algorithms that scan the entire EUVI database. At the time of writing, there exist clear indications of more such events. For instance, a search of EIT wave events during the STEREO epoch revealed some 34 candidates, of which 7 events have been studied so far (David Long, presentation at SECCHI consortium meeting, October 2008). Inspecting the spacecraft separation angle in Table 1 we see that 9 events have been observed at separation angles of $\alpha_{sep} \approx 6^\circ - 47^\circ$ and are thus suitable for stereoscopic 3D reconstruction.

2.5 Stereoscopic Fitting of Circular Loop Geometry

One of the 10 STEREO-observed events listed in Table 1, with loop oscillations occurring during the 2007-Jun-27, 17:30 UT, flare, has already been analyzed in Verwichte et al. (2009) and Aschwanden et al. (2009). We are focusing here on the reconstruction of the 3D geometry of the same oscillating loop. No stereoscopic 3D reconstruction with a triangulation method has been attempted in the first study on this loop, because

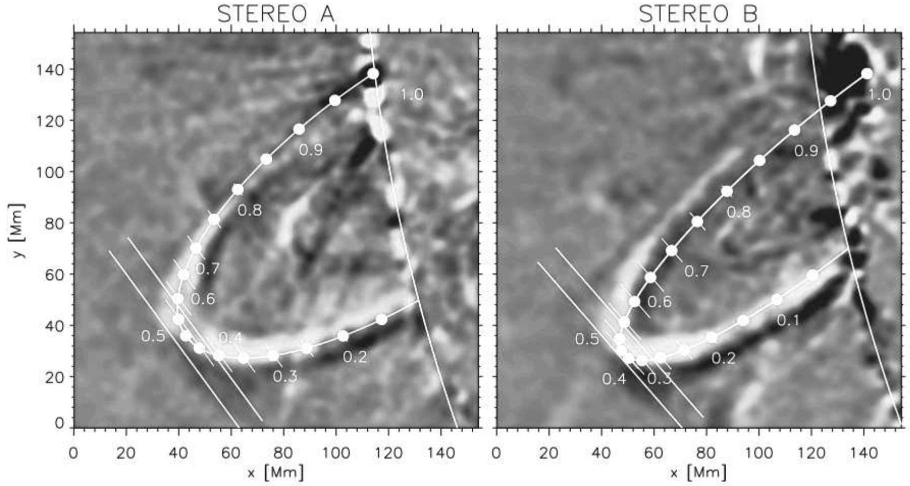

Fig. 4 3D reconstruction of an oscillating loop observed during the flare of 2007-Jun-27, $\approx 18:19$ UT, superimposed on the STEREO/A (left) and STEREO/B images (right), using the *dynamic stereoscopy method* [from Verwichte et al. 2009].

the loop footpoints are not visible in one spacecraft (STEREO/A), cannot easily be located in the image of the other spacecraft (STEREO/B), as well as corresponding features of the upper loop segment are difficult to verify in both images, and thus the technique of *dynamic stereoscopy* was applied (Verwichte et al. 2009). Essentially, a semi-circular geometry was fitted to the loop by varying the inclination angle of the loop plane, leading to a loop radius of $r_{loop} = 110$ Mm, an azimuth angle (of the loop baseline) of $\alpha = 29^\circ$ (anti-clockwise from the heliographic east-west direction), and an inclination angle of $\theta = 27^\circ$. The 2D projection of this 3D geometry in the LOS directions of STEREO/A and B is shown in Fig. 4.

2.6 Stereoscopic Triangulation of an Oscillating Loop

We employ now the stereoscopic triangulation method, which has been applied to STEREO/EUVI data before, e.g., to some 70 active region loops observed with EUVI/A and B on 2007-May-09 (Aschwanden et al. 2008a,b,c), as well as to two other active regions (with each 100-200 loops) observed with STEREO/EUVI on 2007-Apr-30 and May 19 (Sandman et al. 2009; DeRosa et al. 2009).

Before stereoscopic triangulation can be carried out, some preprocessing steps are required that coalign the two STEREO/A and B images to identical pixel size (or identical distance to the Sun), identical orientation (or identical spacecraft roll angle with respect to the solar axis), with one image axis coplanar to the epipolar plane (i.e., the plane that intersects the Sun center and the two spacecraft A and B positions, pointing approximately in east-west direction in the ecliptic plane; for a definition see Inhester 2006). Once the two images have been properly aligned, with the x-axis of the images parallel to the epipolar plane, stereoscopic triangulation can straightforwardly be carried out by measuring the x-parallax of epipolar loop points.

The geometry of a loop point P with position x_A in the EUVI/A image and position x_B in the EUVI/B image for an epipolar point is shown in the x-z plane in Fig. 5. The loop position P is observed at the image coordinates (x_A, y_A) from spacecraft A,

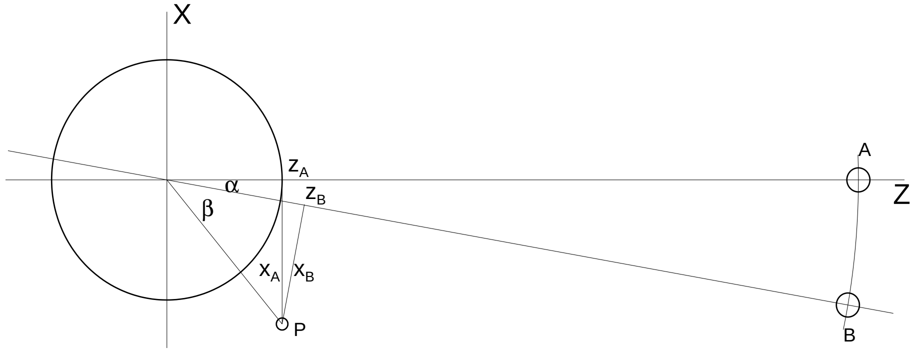

Fig. 5 Geometry of an epipolar point (P) in the plane $y = y_A = y_B$ with respect to Sun center and the spacecraft positions A and B. The spacecraft A and B have a separation angle α and measure a position x_A, and x_B with respect to their line-of-sight through Sun center. The 3D position z_A can be triangulated from the observables x_A, x_B, $y_A = y_B$, and α.

and (x_B, y_B) from spacecraft B, respectively, where the y-coordinate is perpendicular to the epipolar x-z plane $(y = y_A = y_B)$ depicted in Fig. 5. The two spacecraft A and B have a separation angle α, and the relation to the longitude angle β of point P seen by spacecraft B is given by the two geometric relations

$$\sin(\alpha + \beta) = \frac{x_A}{\sqrt{(x_A^2 + z_A^2)}} \ , \tag{7}$$

$$\sin(\beta) = \frac{x_B}{\sqrt{(x_A^2 + z_A^2)}} \ . \tag{8}$$

Applying the additive theorem for the sine function, i.e., $\sin(\alpha + \beta) = \sin(\alpha)\cos(\beta) + \cos(\alpha)\sin(\beta)$, we obtain a quadratic equation for the LOS distance z_A that has the following two algebraic solutions,

$$z_A = \pm\sqrt{\left(\frac{x_A - x_B\cos(\alpha)}{\sin(\alpha)}\right)^2 + \left(x_B^2 - x_A^2\right)} \ . \tag{9}$$

The two solutions refer to the east-west symmetry and a geometric consideration of the special case $\cos(\alpha) = x_B/x_A$ reveals that the sign of z_A depends on the sign of $\cos(\alpha)$. Thus, we find,

$$\begin{array}{lcl} z_A > 0 & \text{if} & x_B > x_A \cos(\alpha) \\ z_A = 0 & \text{if} & x_B = x_A \cos(\alpha) \\ z_A < 0 & \text{if} & x_B < x_A \cos(\alpha) \ . \end{array} \tag{10}$$

Therefore, we can determine the third coordinate z_A with Eq. (9) and rule Eq. (10) from the measurements of x_A, x_B, and α. To obtain the height h of the loop position P, we need to include also the epipolar coordinate y_A, yielding

$$h = r - R_\odot = \sqrt{x_A^2 + y_A^2 + z_A^2} - R_\odot \ . \tag{11}$$

We carried out a 3D reconstruction of an oscillating loop observed on 2007-Jun-27, 18:19 UT (shown in Fig. 4), with STEREO spacecraft A and B and show the

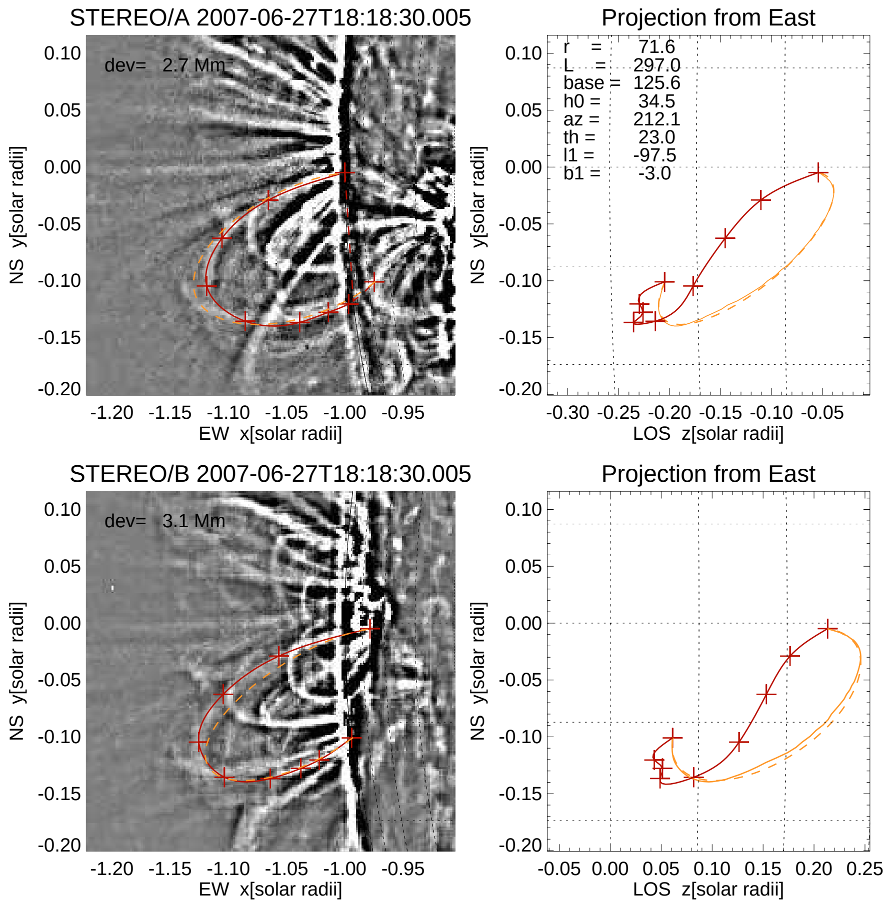

Fig. 6 3D reconstruction of the same oscillating loop as Fig. 4, observed on 2007-Jun-27, 18:19 UT, superimposed on a highpass-filtered image of STEREO/A (bottom) and STEREO/B image (top), using the *stereoscopic triangulation method*. The loop shape is traced with 9 points (red crosses), interpolated with a 2D spline (red curve), and fitted with an elliptical geometry (yellow curve). The circular model (yellow curve) and the solution of the 3D reconstruction (red curve) is also projected into the (z, y) plane (right panels), with z being the LOS.

results in Fig. 6. A number of 9 loop positions (x_A, y_A) have been manually traced in a highpass-filtered image EUVI/A (Fig. 6, top, cross symbols), as well as the corresponding positions x_B at identical epipolar coordinates $y_B = y_A$ in image EUVI/B (Fig. 6, bottom, cross symbols). [As a footnote: The oscillating loop can be identified best in a running-difference image, as shown in Fig. 4, but the coordinates can be measured more accurately in a highpass-filtered image, as shown in Fig. 6.] The loop coordinates are then interpolated with 8-times higher resolutions with a 2D-spline fit (solid red curve in left panels of Fig. 6). The stereoscopic triangulation of the positions (x_A, x_B) with spacecraft separation angle $\alpha = 8.2628°$ at that time yields then with Eqs. (9-11) the z_A coordinates along the line-of-sight, and the heights h for each loop position. We display projections orthogonal to the line-of-sight of EUVI/A and

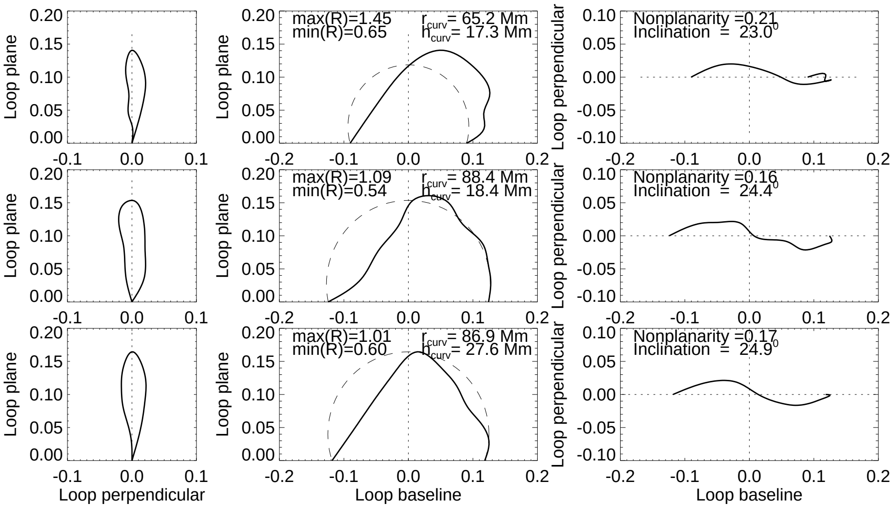

Fig. 7 Projections of the reconstructed 3D loop geometry (see Fig. 6) into the 3 orthogonal planes of the loop coordinate system: edge-on (left), side-on (middle), and top-down (right). The three rows present 3 independent trials of manual loop tracings.

EUVI/B in Fig. 6, both in the y-z plane (Fig. 6, right panels). We repeat the tracing three times to obtain an empirical uncertainty of the triangulation method. The three solutions of the triangulated loop are shown together in Fig. 7 (thick black curves). Surprisingly, the triangulated loop reveals an S-shaped geometry in the vertical projection top down (Fig. 7, right panel), and a heavily deformed asymmetry in the side-on projection (Fig. 7, middle panels). Thus, the oscillating loop seems to be neither circular nor coplanar. This is an intriguing new result that could not have been obtained without the STEREO observations.

If we fit a circular geometry to the same 2D loop tracings (dashed yellow curves in Fig. 6), we obtain from the average and standard deviations of 3 independent tracings the following parameters: a baseline azimuth angle of $\alpha = 27.0^\circ \pm 4.5^\circ$, a loop plane inclination angle of $\theta = 24.1^\circ \pm 1.0^\circ$, a loop radius of $r = 83 \pm 10$ Mm, and a full loop length of $L = 319 \pm 19$ Mm. The full 3D loop length of the triangulated loop is slightly shorter than the circular model, i.e., $L = 311 \pm 22$ Mm. This compares favorably with the semi-circular forward-fitting of Verwichte et al. (2009), who obtained values of $\alpha = 19^\circ$, $\theta = 27^\circ$, $r = 110$ Mm, and $L = 346$ Mm. Thus, we conclude that the circular forward-fitting model yields values that are very close to those of the stereoscopic method, differing by $\approx 3^\circ$ for the loop plane inclination angle and by $\approx 10\%$ for the loop length, which is the most important parameter for coronal seismology. However, the forward-fitting model makes the assumption of circularity and coplanarity, and thus cannot reveal asymmetric and nonplanar shapes of the oscillating loop.

In Fig. 7, we transformed the loop coordinates from the image coordinate system (x_A, x_B, x_Z) into the loop coordinate system (X, Y, Z), which is defined in the following way: the horizontal X-axis is aligned with the loop baseline between the two loop footpoints, with the midpoint as center X=0. The vertical Z-axis intersects the baseline midpoint and the apex midpoint of the loop, while the Y-axis is perpendicular to the X-Z plane. The coordinate transformation is accomplished by 3 subsequent rotations (i.e., by the azimuth angle α, the loop plane inclination angle θ, and the longitude angle l_1, see §3.4.4. in Aschwanden 2004). The oscillating loop shown in Fig. 7 is clearly heavily deformed and deviates significantly from a coplanar and circular model. The maximum deviations Δr from the average loop radius r are $0.54 < (\Delta r/r) < 1.45$, and the nonplanarity reaches up to $\lesssim 0.21$ of the loop radius, which is much larger than for typical active region loops, which have radial variations of $\lesssim 1.2$ and nonplanarity deviations of $\lesssim 0.1$ (see Fig. 9 in Aschwanden et al. 2008a). Obviously, this loop is highly non-circular and non-planar, possibly affected by the dynamic magnetic forces associated with the launch of a CME that usually is responsible for triggering loop oscillations.

2.7 Cross-sections of Oscillating Loops

In the common fluxtube concept of coronal loops, the 3D geometry can be broken down into two parts: (1) the 3D geometry of the loop axis $\mathbf{x}(s) = [x(s), y(s), z(s)]$ (with s the length coordinate along the loop), and (2) the cross-sectional area function $A(s) \approx w^2(s)$, which can be characterized by an average width $w(s)$, but may vary along the loop. In a cylindrical fluxtube model, a circular cross-section is assumed with a constant radius. However, the concept of a cross-sectional area or radius implies a step function in density,

$$n(r) = \begin{cases} n_i \text{ for } & r < a \\ n_e \text{ for } & r \geq a \end{cases} , \tag{12}$$

where n_i represents the internal density, n_e the external density, and a is the circular loop radius. A step function for the radial density function represents the simplest mathematical model, but a more refined model with finite density gradients is important for theoretical models that explore the damping of oscillations by resonant absorption or phase mixing (Goossens 1991; Poedts 2002; Ruderman & Roberts 2002; Ofman & Aschwanden 2002; Goossens, Andries, & Aschwanden 2002; Erdélyi 2003). In the studies of Ruderman & Roberts (2002), the cross-sectional density function has been parameterized with an approximately trapezoidal function, where the edges are smoothed with a sine function,

$$n(r) = n_i \begin{cases} 1 & \text{for} \quad r < (a-l) \\ (1+\chi)/2 - (1-\chi)/2 \ \sin[(\pi/2)(2r+l-2a)/l] & \text{for} \quad (a-l) < r < a \\ \chi & \text{for} \quad r > a \end{cases} , \tag{13}$$

where $\chi = n_e/n_i$ is the density ratio, a the outer loop radius, and l the skin depth (containing the density gradient). This cross-sectional function $n(r)$ has been fitted to 11 oscillating loops and a mean density ratio of $\chi = n_e/n_i \approx 0.30 \pm 0.16$, a mean outer loop radius of $a = 4.5 \pm 3.5$ Mm, and a mean skin depth of $l = 3.9 \pm 3.1$ Mm was found (Aschwanden et al. 2003), which corresponds to a skin depth ratio of $l/a \approx 0.87 \pm 1.08$. The best-fit density profiles $n(r)$ are shown in Fig. 8. This means that the density varies almost over the entire loop cross-section, and thus the trapezoidal-sinusoidal geometry almost degenerates to a gaussian cross-section. This has severe consequences for the damping of loop oscillations, making resonant absorption very efficient.

In deducing the loop cross-sectional density profiles, one has to convolve a theoretical density profile $n(r)$ with the line-of-sight depth $z(r) \approx \sqrt{(a^2 - r^2)}$ to obtain the radial emission measure profile $EM(r) \approx n(r)^2 z(r)$, and then convolve with the

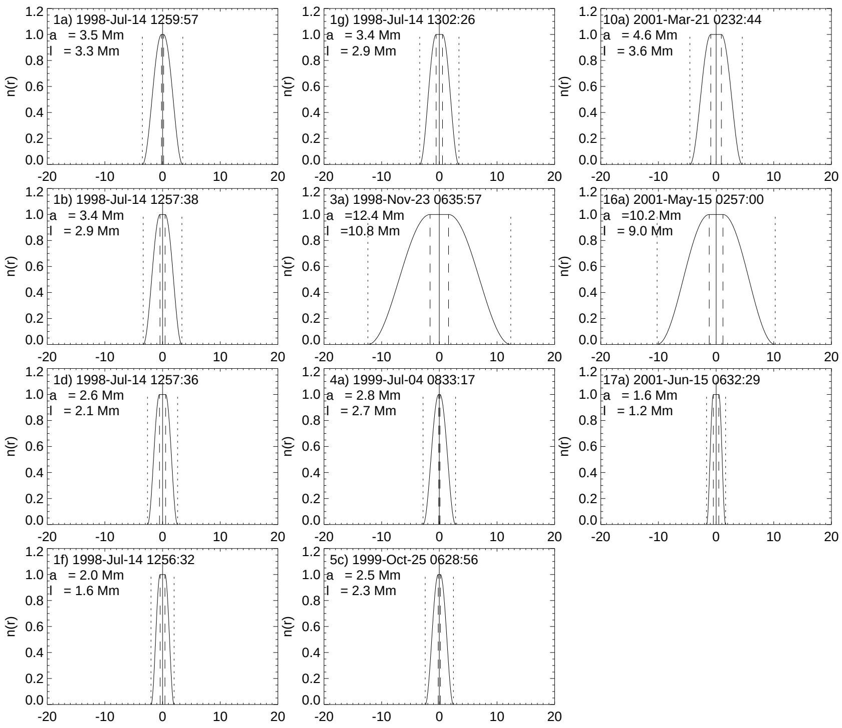

Fig. 8 Best-fit density profiles $n_e(r)$ as function of radial distance from loop center for 11 oscillating loop events. The dates of the events and the best-fit parameters a and l are indicated in each panel. Each profile is averaged from 10-30 timesteps during the time interval of the observed loop oscillation [from Aschwanden et al. 2003].

instrumental point spread function $PSF(r)$, which both have a smoothing effect. As a consequence, the two convolutions do not allow to determine the intrinsic density profile $n(r)$ with high accuracy. In fact, a rectangular step function, a sinusoidal, or a gaussian density profile $n(r)$ cannot be discriminated in unresolved or marginally resolved loops (see Fig. 1 in Aschwanden, Nightingale, & Boerner 2007). Since most elementary loop threads (with isothermal cross-sections) have typical diameters of $w \approx 1.5$ Mm, which are barely resolved with TRACE ($w_{PSF} \approx 0.9$ Mm), instruments with higher spatial resolution are required to measure loop cross-sectional profiles reliably.

Another geometric characterization is the variation of the loop width with length, $w(s)$. Most measurements of loop width variations show only slight variations in the order of typically 10%-20% (e.g., Klimchuk 2000; Aschwanden et al. 1999a), which is significantly less than expected for a dipolar magnetic field model, as well as for twisted configurations (Klimchuk et al. 2000), and thus remains an unexplained mystery at this time. Theoretical calculations of nonaxisymmetric oscillations in twisted fluxtubes show that the twist does not affect the kink mode (Ruderman 2007). The tube expansion factor (i.e., the ratio of the fluxtube radii at the apex and footpoints), however, affects the determination of the density scale height based on the fundamental/harmonic ratio

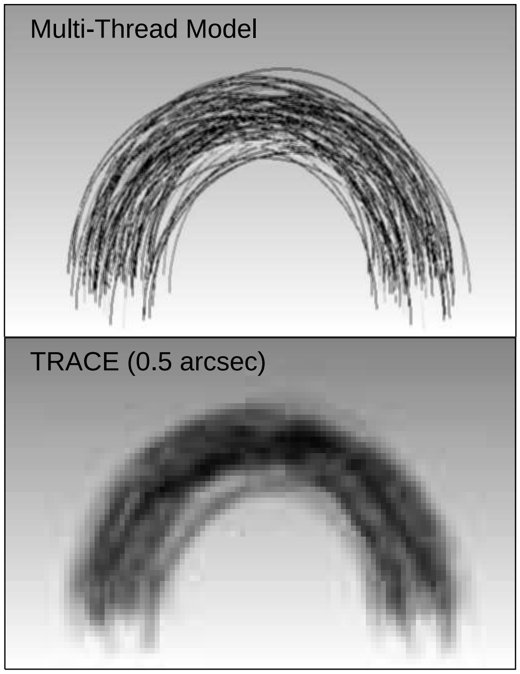

Fig. 9 The concept of a multi-thread loop model is visualized with a bundle of 100 fine loop threads with a width of $0.1''$, random footpoint positions, and random fluxes. The top panel shows the simulated image with a pixel size of $0.1''$, while the bottom panel renders the loop system with a degraded resolution of $0.5''$, similarly as the TRACE telescope would see it. [from Aschwanden, Nightingale, & Alexander 2000].

of the kink-mode period (Ruderman, Verth & Erdélyi 2008; Diaz, Donnelly, & Roberts 2007).

2.8 Finestructure of Oscillating Loops

The generic fluxtube model of loops entails a cylindrical geometry with some curvature, but assumes a homogeneous density (across the cross-section) with a filling factor of unity. While loop threads with diameters of $w \approx 1-2$ Mm indeed have been found to be near-isothermal and homogeneous (Aschwanden & Nightingale 2005), oscillating loop systems with larger diameters have been observed that presumably consist of bundles of loop threads, and thus are inhomogeneous in density and temperature (Fig. 9). Often we observe an isolated oscillating loop system, consisting of a single loop or a bundle of loop threads (or strands), but sometimes all loops of an active region are displaced and involved into oscillations with various amplitudes (Fig. 10). Other examples of complex oscillating loop systems are given in VanDoorsselaere, Nakariakov, & Verwichte (2007) and DeMoortel & Brady (2007), which show multiple loop threads involved in each oscillation episode. Whatever the oscillating system is, defined by a coherent oscillation amplitude and period, any finestructure could significantly affect

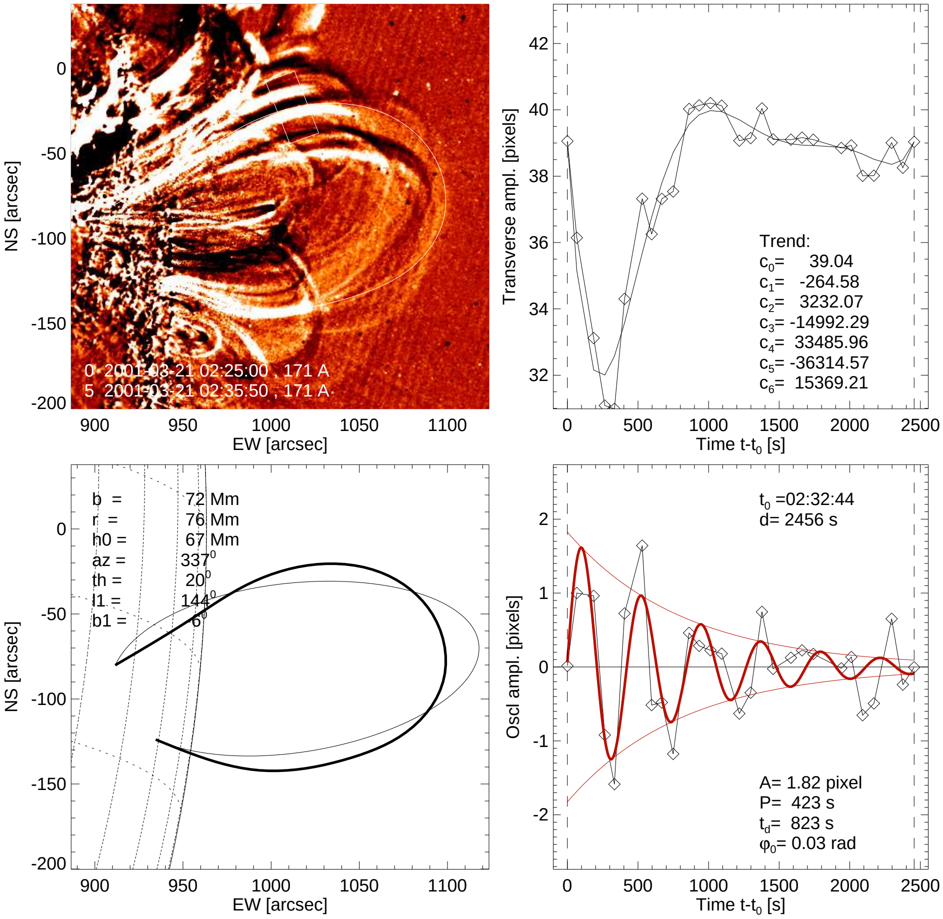

Fig. 10 Oscillation event of 2001 March 21, 02:32 UT: running-time difference image of TRACE 171 Å(top left); fit of a circular loop geometry (bottom left); absolute oscillation amplitude (top right) measured in box shown in top left panel; and detrended oscillation amplitude fitted with an exponential decaying sine function. Note that all loops of the entire active region are displaced in the running-time difference image. [from Aschwanden et al. 2002].

the kink-mode periods, the coherence and oscillation phases of neighbored loop threads, or the damping rate of the oscillating loop system.

Kink-mode oscillations with vertical polarization of a multi-stranded loop system (with up 5 loop strands) have been simulated numerically (2D) by Gruszecki et al. (2006), where very closely-spaced loop strands were found to change the collective kink oscillation behavior, while more distant strands oscillated independently. The collective behavior of two adjacent slabs was also analyzed by Luna et al. (2006, 2008), who find that the normal modes of the coupled slab system is different from the modes of an individual slab and that both the fundamental symmetric (sausage-type) and antisymmetric (kink-type) mode can be excited at the same time. The influence of internal loop structuring on resonant damping of kink-mode oscillations was studied by Arregui et al. (2007) and Terradas et al. (2008), who found only minor ($\lesssim 15\%$)

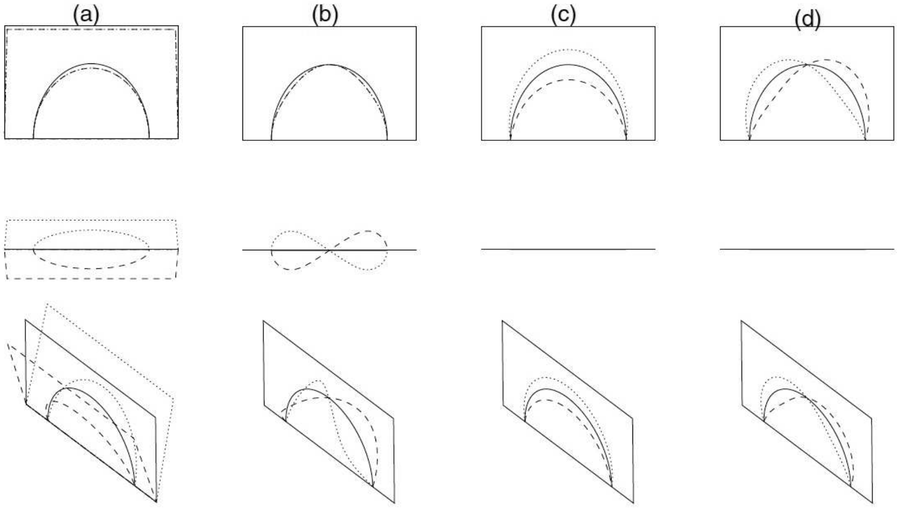

Fig. 11 Classification of kink-mode oscillations into 4 cases, according to their fundamental (a and c) or harmonic number (b and d), and their polarization in horizontal (a and b) and vertical direction (c and d) [from Wang, Solanki, & Selwa 2008].

changes in the kink-mode period and damping for two closely-spaced loop threads of equal density, but the changes could be much larger for loop threads with different densities. Numerical simulations of impulsively excited magnetosonic waves in parallel slabs also demonstrated that adjacent strands affect wave propagation and the resulting spectra (Ogrodowczyk & Murawski 2007). All these studies underscore that the (so far purely understood) finestructure of loops has significant influence on oscillations, wave propagation and wave damping, and thus needs to be studied in more detail, based on realistic models of the inhomogeneous loop finestructure.

3 The 3D Motion of Oscillating Loops

While we introduced 3D reconstruction methods of coronal loops in §2, which are applicable to stationary loops as well as to oscillating loops, we explore now the 3D motion in the time domain. While we previously discussed how to determine the 3D coordinates $\mathbf{x}(s) = [x(s), y(s), z(s)]$ of a loop from a particular image, which was taken as a snapshot at a particular time t, we like to explore now the time dependence $\mathbf{x}(s,t) = [x(s,t), y(s,t), z(s,t)]$, which should allow us also to determine 3D velocities $\mathbf{v}(s,t) = d\mathbf{x}(s,t)/dt$ and 3D acceleration vectors $\mathbf{a}(s,t) = d^2\mathbf{x}(s,t)/dt^2$.

3.1 Previous Measurements of the 3D Motion of Oscillating Loops

Most previous studies measured only the amplitude $A(t)$ of kink-mode oscillations in the 2D projection of the image plane, preferentially in perpendicular direction to the loop axis (e.g., Aschwanden et al. 1999b; Nakariakov et al. 1999). For instance, the oscillation amplitude $A(t)$ shown in Fig. 2 (bottom right panel) is measured in a box perpendicular to the loop axis as shown in the image in Fig. 2 (top left panel). Although

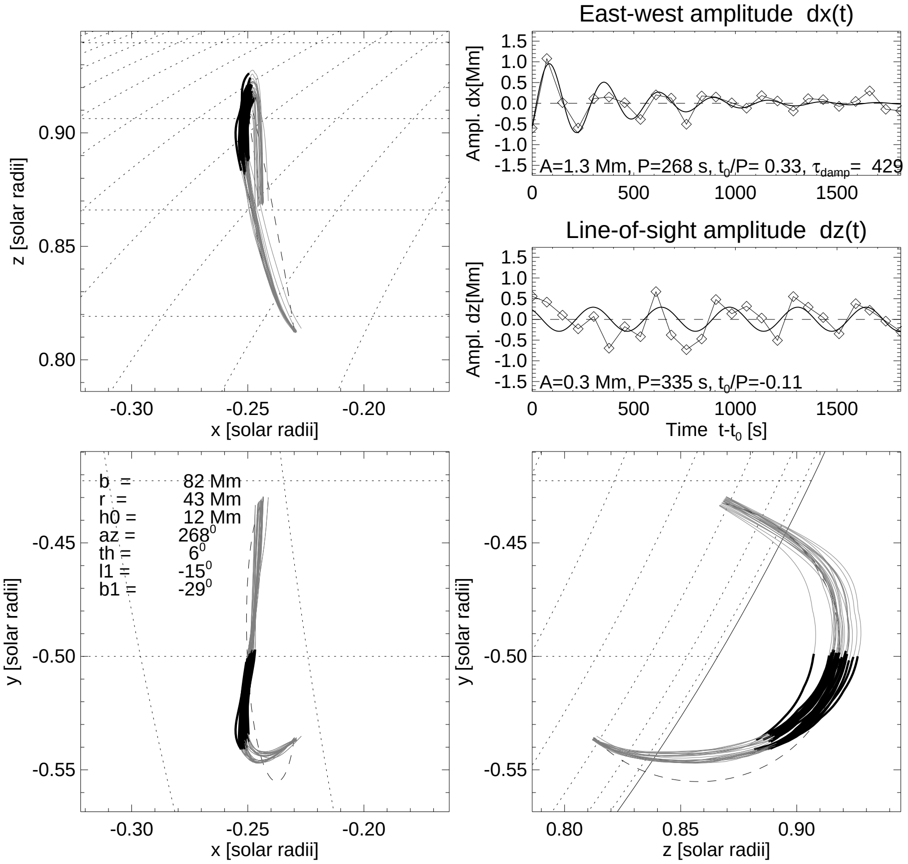

Fig. 12 3D reconstruction of loop oscillations for a sequence of TRACE 171 Å images in the time interval of 1998-Jul-14, 12:59-13:35 UT (identical time interval of shown in Fig. 2). The method of the 3D loop geometry with the curvature maximization method is visualized similar to Fig. 3, with the loops traced at different times rendered as grey curves. In addition we show the average loop amplitude $dx(t)$ in the horizontal x-direction and $dz(t)$ in the vertical z-direction (top right panels), for the middle loop segment (in the segment $0.5 < (s/L) < 0.8$, marked with black curves), as well as a fit of an exponentially damped sine function to the observed time profiles [see movie at *http://www.lmsal.com/˜aschwand/movies/TRACE/T171_980714_osc.mov*].

we expect that the unknown polarization of the oscillation plane should not affect the kink-mode period, there is an ambiguity in what plane the loop oscillates. Evidence that not all loops execute transverse (horizontal) oscillations, but can also oscillate in a vertical plane to the solar surface, was first shown by Wang & Solanki (2004) and studied systematically by Wang, Solanki, & Selwa (2008). The motion of kink-mode oscillations was classified into 4 categories, depending on the fundamental/harmonic mode and the horizontal/vertical polarization (Fig. 11). From a sample of 14 loop oscillations they were able to classify 3 cases as fundamental horizontal mode, 2 cases as fundamental vertical mode, 1 case as horizontal/vertical combination, while the other 8 cases were ambiguous (Wang et al. 2008). The reason for ambiguous classification could be related to an unfavorable projection direction or due to a more complicated motion, such as torsional or other non-symmetric motions.

3.2 3D Motion Modeled with the Maximum Curvature Method

Since no general method has been developed yet to study the 3D motion of oscillating loops, we explore here whether the *curvature maximization method* described in §2.3 is suitable to reconstruct the 3D motion from 2D images. This model of the 3D geometry of a loop is fully consistent with the observed 2D projection coordinates (which is often not the case for circular loop models), while we make the only assumption of maximum possible curvature radius in 3D space to retrieve the third coordinate in the line-of-sight. The method is fully described in §2.3, and an example for a snapshot at a given time is shown in Fig. 3. We repeat now the 3D reconstruction of the loop coordinates $[x(s,t_i), y(s,t_i), z(s,t_i)]$ for a time series $t_i = 1,..,29$ of the loop oscillation event during the 1998-Jul-14, 12:59-13:35 UT flare time interval, shown in Fig. 2 (bottom right panel). For each of the 29 TRACE 171 Å images we trace the loop coordinates $[x(s,t_i), y(s,t_i)]$ (of the loop selected in Fig. 2) and perform a 3D reconstruction of the line-of-sight coordinate $z(s,t_i)$ with the curvature minimization method (Eqs. 3-6) as shown in Fig. 3. The combined results from all 29 loop positions are shown in Fig. 12 (rendered as grey curves): in the observed x-y image plane (Fig. 12, bottom left), in the reconstructed x-z plane edge-on to the the loop (Fig. 12, top left), and in the reconstructed z-y plane side-on to the loop (Fig. 12, bottom right). For a loop segment $0.5-0.8$ times the loop length (marked with black segments in Fig. 12) we measure the average loop amplitude $dx(t)$ in horizontal (parallel to x-axis) direction, shown in the right top panel in Fig. 12, which exhibits the well-known kink-mode oscillation. Fitting an exponentially damped sine-function to the horizontal amplitude (after subtracting a linear trend by a regression fit),

$$dx(t) = A_0 \cos\left(\frac{2\pi(t-t_0)}{P}\right) \exp\left(-\frac{(t-t_0)}{\tau_{damp}}\right) , \tag{14}$$

we find an initial amplitude of $A_0 = 1.3$ Mm, a period of $P = 268$ s, a damping time of $\tau = 429$ s, and a phase of $t_0/P = 0.33$. This compares to similar values in the original analysis ($A_0 = 0.8$ Mm, $P = 261$ s, and $\tau_{damp} = 1183$ s; Aschwanden et al. 2002). The slight differences originate from the choice of slightly different loop locations in the oscillation measurements. The largest uncertainty is in the measurement of the damping time, because of the noise in the oscillation amplitudes resulting from temporal fluctuations of the background.

Since we reconstructed the 3D geometry with the curvature minimization method, we can also study the vertical motion $z(s,t)$, which we show averaged over the the same segment $0.5 < s/L < 0.8$ and after removal of a linear trend, i.e., $dz(t)$ in Fig. 12 middle right panel. We fit also an exponentially damped sine-function to the vertical motion $dz(t)$ with Eq. (14) and find an initial amplitude of $A_0 = 0.3$ Mm, a period of $P = 335$ s, a undetermined damping time, and a phase of $t_0/P = 0.11$. This is a surprising result, since we do not expect any significant vertical oscillatory motion for a transverse (horizontal) kink-mode oscillation. There are three striking new properties we are finding here: (1) The oscillation period P of the vertical and horizontal motion agrees approximately, so the vertical and horizontal motions are correlated, as one would expect for a polarized motion (with an oscillation plane in a different direction than the observed horizontal one); (2) The amplitude of the vertical oscillation is smaller than the horizontal motion, so the plane of oscillation is mostly horizontally polarized; and (3) the vertical motion has a time lag of $\Delta t_0/P = 0.11 - 0.33 = -0.22$ (kink-mode) periods. This complicated motion is a combination of polarized and torsional modes, because linear polarization would lead to a combination of horizontal and vertical modes with no phase delay, while the torsional model introduces a phase delay between orthogonal directions. The deviations from a standard kink-mode motion in transverse (horizontal) direction may be caused by the nonplanar and noncircular loop shape, which is in first place dictated by the local magnetic forces in the corona, that produce such a particular loop shape (as shown in in Fig. 3) in a force-free equilibrium before the loop oscillation gets excited. Interestingly, the same loop (case 1a in Aschwanden et al. 2002) was classified as fundamental horizontal oscillation in Wang et al. (2008), in their category III of loops located on disk and loop plane nearly parallel to LOS. Wang et al. (2008) say that horizontal and vertical oscillations for this orientation look similar, but can easily be distinguished from each other. Here, we find a combination of horizontal and vertical polarization. Since the oscillations in the two directions has the same period but a phase delay of about a quarter of a period, the motion may correspond to a torsional mode. The difference in this conclusion lies in the fact that Wang et al. (2008) assume coplanar loops and omit torsional modes, while we allow for nonplanarity and torsional modes, requiring the maximum curvature condition only, which is inherent to force-free magnetic fields.

3.3 3D Motion Reconstructed from Stereoscopic Observations

Using the method stereoscopic 3D triangulation, as shown for a single time frame at 2007-Jun-27, 18:18:30 UT in Fig. 6, we repeat now the same procedure for 12 (epipolar-coaligned) stereoscopic image pairs in the time interval of 17:58-18:26 UT. The same time sequence is shown in form of running-time difference images in Fig. 16 of Aschwanden et al. (2009), yielding an oscillation period of $P = 565$ s and an exponential damping time of $\tau_{damp} \approx 1600$ s (Fig. 17 of Aschwanden et al. 2009). The triangulated 3D geometry of the oscillating loop is shown in Fig. 13, which has a consistent asymmetric S-shape throughout the entire observed time interval (≈ 35 min) as shown in Fig. 6, while the oscillation amplitude is much smaller than the deviations of the loop geometry from a circular model. We display the average amplitude of loop motions in x-direction (east-west amplitude $dx(t)$ in Fig. 13 top right panel), and in z-direction (line-of-sight amplitude $dz(t)$ in Fig. 13 middle right panel). Both amplitudes show a correlated oscillation with similar periods and amplitudes, i.e. $P = 681$ s for $dx(t)$ and $P = 685$ s for $dz(t)$, and $A_0 = 1.4$ Mm for $dx(t)$ and $A_0 = 1.5$ Mm for $dz(t)$, respectively. The amplitude $dx(t)$ corresponds to an oscillation in the vertical plane (with respect to the solar surface), and $dz(t)$ to an oscillation in the horizontal plane, but the two oscillations are almost in phase ($t_0/P = 0.19$ vs. $t_0/P = 0.26$. The fact that the two oscillation directions have a similar amplitude implies that the polarization is a combination of horizontal and vertical planes with a polarization angle near 45°. The fact that the oscillations in the two planes are almost in phase implies that the kink-mode oscillation could take place in a fixed plane (e.g., linear polarization), say with polarization angle of $\approx 45^\circ$. However, since the average 3D loop geometry corresponds to a nonplanar, helically-twisted shape, the 3D motion can also be described in terms of a torsional

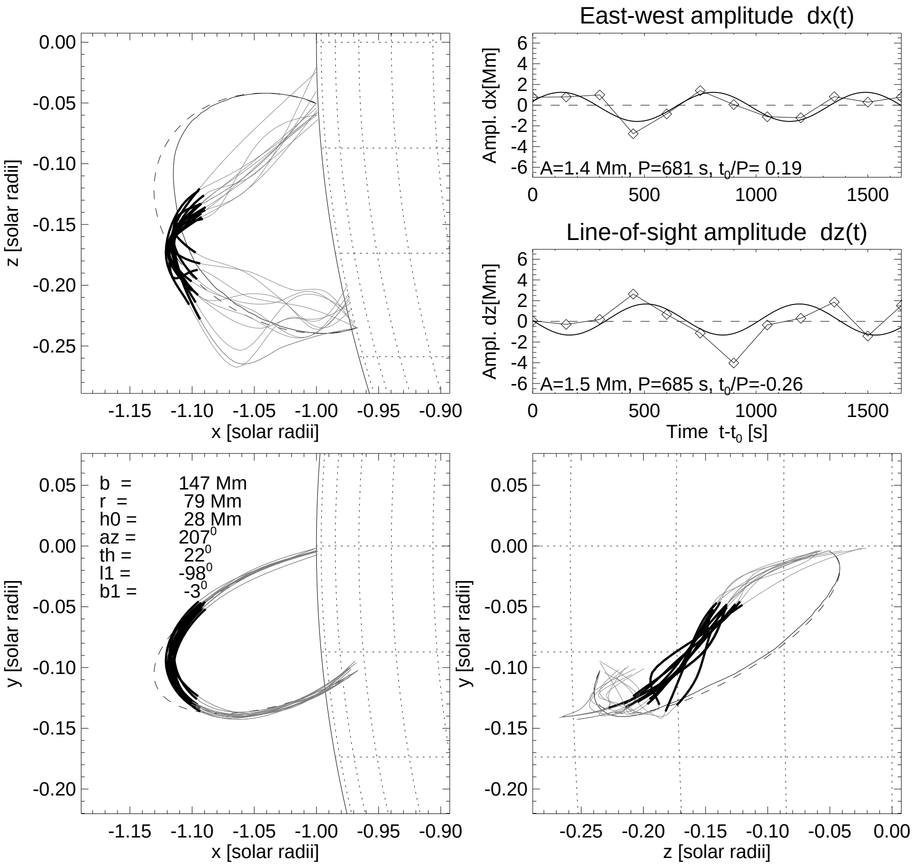

Fig. 13 3D reconstruction of loop oscillations for a sequence of 16 EUVI/A+B 171 Å images in the time interval of 2007-Jun-27, 17:58-18:26 UT, using the stereoscopic triangulation method. The loop tracings in EUVI/A are rendered in the x-y plane (left bottom panel), while the orthogonal reconstruction are shown in the x-z plane (top left panel) and in the z-y plane (bottom right panel). The loop tracings are rendered with grey curves, the semi-circular fit with a dashed curve, and the maximum curvature method with a thin black curve. The oscillation amplitudes averaged in the loop segments $0.3 < s/L < 0.6$ (marked with thick black curves) are shown in x-direction (east-west amplitude $dx(t)$ in top right panel) and in the z direction (line-of-sight amplitude $dz(t)$ in middle right panel). See also movie at *http://www.lmsal.com/˜aschwand/movies/EUVI/ EUVI_20070627_171_osc.mov*].

oscillation (circular polarization). It is instructive to inspect a movie visualization of Fig. 13 (*http://www.lmsal.com/˜aschwand/movies/EUVI/T171_20070627_osc.mov*).

In Fig. 14 we show the triangulated loop motion projected into the 3 orthogonal directions of the loop coordinate system (similar to Fig. 7). In order to illustrate the plausibility of a torsional motion we simulate a helically twisted loop (with a twist of 0.75 turns and geometric tapering of the toroidal radius towards the footpoints) that undergoes a periodical change in the twist angle, where the displacement is highest at the loop apex and falls off towards the footpoints. This simple simulation shown in Fig. 14 (bottom half) demonstrates qualitatively how the observed loop shapes and

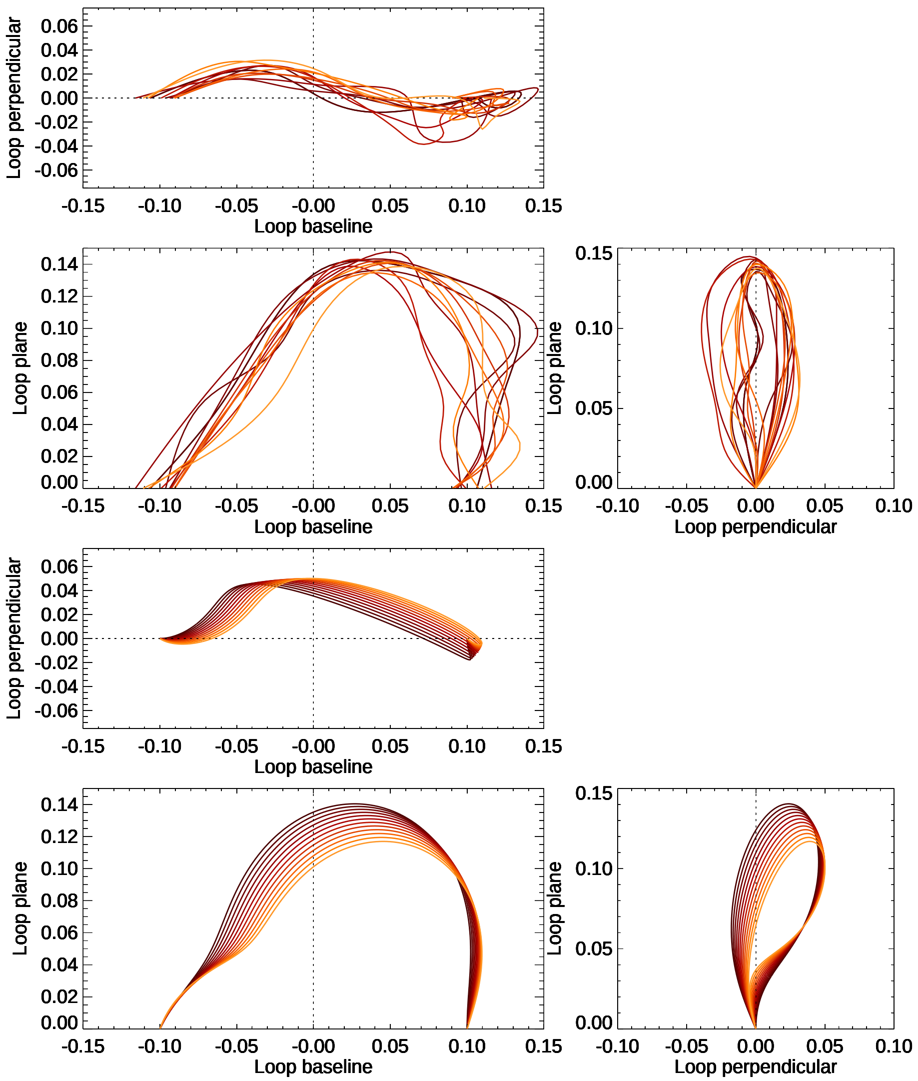

Fig. 14 Orthogonal projections of a triangulated oscillating loop (frames in top half) during the same time interval as shown in Fig. 13 (with the time marked by colors, progressing in order of brown-red-orange-yellow). The bottom panels visualize the same projections of a helically twisted model loop (see model parameters in text). Movie available at *http://www.lmsal.com/˜aschwand/movies/EUVI/ EUVI_20070627_171_3d.mov.*

motions (Fig. 14 top half) can be explained by a toroidal oscillation. Some further modeling studies are required to decide whether we deal with a linearly or circularly polarized oscillation of the kink mode. The helically twisted geometry may also stimulate theoretical theory how linearly polarized kink-modes couple with torsional modes.

3.4 Harmonic Substructures of Oscillating Loops

The 3D motion of a kink-mode oscillation can be further complicated when multiple harmonics $n = 1, 2, ...$ are excited, which represent standing eigen-modes with wavelengths of $\lambda/2 = L/n$. Evidence for such multiple harmonics in transverse kink-mode oscillations was found for the event 1998-Nov-23, 06:35 UT, based on the detection of harmonic periods $P_2/P_1 \lesssim 2$ (VanDoorsselaere, Nakariakov, & Verwichte 2007), but the spatial nodes could not be determined from geometric inference for this loop near the limb, which also seems to be heavily twisted. Evidence for harmonic kink modes from direct detection of the spatial nodes was found for the 2001-May-13 event by DeMoortel & Brady (2007), but strangely no fundamental mode was observed. Since the observed loop has an S-shape in projection, it could be a helical loop twisted by about one turn, which can display torsional oscillations and can mimik almost stationnary nodes for some line-of-sights (see geometric simulation in Fig. 14 bottom). Evidence for harmonics was also found from double peaks in the power spectrum of intensity fluctuations in cool loops at OV wavelengths (O'Shea et al. 2007). We would expect that an asymmetric loop oscillation with a triangular loop shape can be decomposed into spatial Fourier components with dominant peaks in fundamental and lower harmonics (i.e., the third harmonic for a symmetric triangle, or second harmonic for an asymmetric triangle), which could explain the simultaneous detection of harmonic periods. Vice versa, the detection of harmonic peaks in the power spectrum provides a diagnostic for the spatial (asymmetric) loop shape.

The study of harmonic kink-mode period ratios P_2/P_1 has gained particular interest because it provides also a diagnostic for the density scale height in the loop, since the density stratification causes a deviation from the exact ratio $P_2/P_1 = 2$ (Andries et al. 2005; McEwan et al. 2006, 2008; Dymova & Ruderman 2005, 2006). Van Doorsselaere et al. (2007) measured a ratio of $P_2/P_1 = 1.80 \pm 0.05$ and inferred a density scale height of $\lambda = 109$ Mm, which is about the double of the estimated hydrostatic scale height of $\lambda_T \approx 50$ Mm for 1 MK plasma seen at 171 Å. This interesting type of hydrodynamic diagnostic based on coronal seismology could be enhanced and corroborated by spatial measurements of harmonic nodes. However, a statistical study of 14 events was not able to reliably distinguish between fundamental kink-mode with horizontal polarization and second harmonic kink-mode with vertical polarization (Wang et al. 2008). Perhaps our methods of *curvature maximization* applicable to 2D images or *stereoscopic triangulation* applied to STEREO images could shed light into the detection of harmonics.

3.5 The Excitation of Loop Oscillations

The 3D motion of an oscillating loop can be decomposed into an oscillatory component (Eq. 14) as well as into a non-oscillatory component, which is a superimposed motion that steadily drifts into some direction. Virtually all loop oscillations are excited by the launch of a CME, a flare, or an erupting filament (Schrijver et al. 2002), which all undergo a dynamic evolution after a magnetic instability, exerting a Lorentz force on the surrounding plasma (an all the loops therein) that needs to be readjusted to a new equilibrium configuration. The detailed physical mechanism of exciting kink-mode oscillations is not yet understood. It was proposed that the driving force is a flare-generated blast wave, which propagates as a magnetoacoustic pulse and triggers kink-mode oscillations when they hit loops at certain angles (Nakariakov et al. 1999; Ofman 2007). However, this scenario does not explain the selectivity of excitation. A more recent idea deals with vortex shedding in the flow field of a launched CME (Nakariakov et al. 2009). Since CMEs are involved in most cases, exhibiting a considerable dimming in EUV (Aschwanden et al. 1999b, 2009; Bewsher, Harrison, & Brown 2008), it is clear that there is significant mass loss in the lower corona during a CME launch, essentially producing an evacuation inside the volume of the rapidly expanding CME bubble, since the density drops reciprocally with the volume for adiabatic expansion, i.e., $n_e(t) \propto 1/V(t)$ (Aschwanden et al. 2009). Therefore, the excitation of loop oscillations needs to be modeled in the context of magnetic forces, flow fields, and density rarification in a realistic scenario of a CME launch.

On the theoretical side, there exists already a number of hydrodynamic simulations that focus on the geometry and dynamics of the excitation of loop oscillations. The excitation of vertical oscillations of a curved coronal loop have been simulated by Murawski et al. (2005) and Selwa et al. (2005). Which wave modes and wavelengths are excited depends on the position and width of the initial pulse, which can produce distorted and asymmetric kink-mode oscillations (Selwa et al. 2007). In more recent numerical MHD simulations, a magnetically twisted annulus is wrapped around the coronal loop, which introduces an infinite set of body wave modes and surface waves at both the inner and outer edges of the annulus (Carter & Erdélyi 2008).

Observationally, we found that most oscillating loops exhibit also a superimposed systematic motion of the loop centroids into some direction (Aschwanden et al. 2002), which probably reflects the motion of the ambient plasma that is dragged by magnetic Lorentz forces associated with the CME launch. Future studies should investigate the direction of this systematic plasma motion with respect to the flow field of the CME in the lower corona, in order to understand the driving force that excites loop oscillations.

4 The Hydrodynamics of Oscillating Loops

In this section we discuss various hydrodynamic effects in coronal loops that play a role for the detection or modeling of kink-mode oscillations. A new aspect of coronal loops detected in EUV wavelength is their non-equilibrium state, which is generally far away from hydrostatic equilibrium and has largely been ignored in previous studies.

4.1 Density Effects in the Detection of Oscillating Loops

The detection of coronal loop oscillations can be accomplished by (1) time series analysis of intensity fluctuations, (2) correlation tracking of spatial motions, or by (3) the Dopplershift of velocity fluctuations. Kink-mode oscillations can be detected with all three methods.

A time series anaylsis of intensity fluctuations $I(x,y,t)$ at a given position (x,y) will reveal a periodic signal in areas that are swept over by oscillating loops. Since the intensity varies proportional to the squared density n_e and loop diameter w for optically thin wavelengths (such as EUV and soft X-rays), i.e., $I \propto \int n_e^2 dz \approx n_e^2 w$, the intensity modulation for kink-mode oscillations is

$$\frac{\Delta I}{I} = \frac{\int n_e^2 dz}{\int n_{back}^2 dz} \approx \left(\frac{n_e}{n_{back}} \right)^2 \left(\frac{w}{n_\lambda \lambda} \right) \ , \tag{15}$$

where λ is the density scale height, while the number n_λ varies between unity (at disk center) and a few (near the limb). Typically, we expect $n_e \approx 10^9$ cm^{-3}, $n_{back}/n_e \approx 0.2-0.5$, $w \approx 1.5$ Mm, $\lambda \approx 50$ Mm, which yields a contrast of $\Delta I/I \approx 0.1-0.8$. This contrast value is generally quite above the photon noise or the detector sensitivity, and thus kink-mode oscillations should be easy to detect with automated algorithms. However, if the intensity is measured in an area that is larger than the oscillation amplitude, the loop is not resolved with respect to the background and no modulation occurs. This is the reason why kink-mode oscillations were not discovered with low-resolution imagers. Typical kink-mode amplitudes in coronal loops are $A \approx 4 \pm 1$ Mm (Aschwanden et al. 1999a), which requires a spatial resolution of $\lesssim 5''$. This could be the reason why extensive earlier searches in Yohkoh data (with $5''$ resolution) brought only marginal evidence for loop oscillations (McKenzie 1997). Recent automated searches with TRACE and EUVI data (with $1''$ and $3''$ resolution) in form of coronal periodmaps (Nakariakov & King 2007), with pixelized wavelet filtering methods (Sych & Nakariakov 2008), or optical flow methods (Gissot & Hochedez 2008), were more successful in detecting transverse and longitudinal loop oscillations. Such automated search methods may be of crucial importance for the overwhelming future database of the *Solar Dynamics Observatory (SDO)*. However, there are limits to spatial detection of oscillations. For instance, the waves that have been detected in Dopplershift with the *Coronal Multi-Channel Polarimeter (CoMP)* at NSO (Tomczyk et al. 2007), which have been interpreted in terms of kink-mode oscillations (VanDoorsselaere, Nakariakov, & Verwichte 2008), correspond to extremely small oscillation amplitudes (rather like *vibrations*), which can be estimated from the ratio of the amplitudes and velocities measured with CoMP and TRACE, i.e.,

$$\frac{A_{CoMP}}{A_{TRACE}} = \frac{v_{CoMP}}{v_{TRACE}} \ , \tag{16}$$

which yields with $A_{TRACE} \approx 4000$ km, $v_{TRACE} = 2\pi A_{TRACE}/P \approx 80$ km s^{-1}, $P \approx 300$ s, $v_{CoMP} \approx 1$ km s^{-1}, an estimated amplitude of $A_{CoMP} \approx 50$ km or $0.07''$, which is far beyond any current imaging capability. In this case, the detection is easier by measurements of the Dopplershift, a method that was also proposed to detect torsional oscillations of coronal loops (Zaqarashvili 2003).

Another density effect that helps to detect loop oscillations is the variation of line-of-sight depths, since each segment of an oscillating loop is subject to a varying aspect angle with respect to the observer's line-of-sight, unless a loop segment is exactly perpendicular to the line-of-sight. This modulational effect scales linearly with the column depth $\Delta z(t)$ along the line-of-sight, and with the cosine of the aspect angle $\psi(t)$, defined between a loop segment and the line-of-sight,

$$I(t) \propto n_e^2 \Delta z(t) \propto n_e^2 \frac{w}{cos(\psi[t])} \ . \tag{17}$$

This effect is more pronounced for harmonic than for fundamental kink-modes (Cooper, Nakariakov, & Tsiklauri 2003), and equally matters for detection of torsional oscillations.

Density variations would be strongest for the sausage-type fast magnetosonic mode (Nakariakov, Melnikov, & Reznikova 2003; Aschwanden, Nakariakov, & Melnikov 2004; Pascoe, Nakariakov, & Arber 2007a,b), because the loop undergoes a radial oscillation that varies the cross-sectional area $A(t)$ as the square of the loop diameter, i.e., $A(t) \propto$

$w(t)^2$, which modulates the density reciprocally to conserve the particle number, i.e., $n_e(t) \propto 1/A(t) \propto w(t)^{-2}$, while the intensity is then modulated with the third power of the radial variation,

$$I(t) \propto n_e(t)^2 w(t) \propto w(t)^{-4} w(t) \propto w(t)^{-3} \ . \tag{18}$$

Therefore, the radial variation is strongly amplified in the intensity modulation, and thus sausage-mode oscillations should be easy to detect. However, the intensity modulation is only prevailing in imaging observations when the loop width is resolved, while the emissivity is less modulated in unresolved observations.

4.2 Effects of Gravitational Stratification

A large fraction of coronal loops, despite their intricate dynamics driven by episodic heating and subsequent cooling, possess a vertical density structure that is close to gravitational stratification of hydrostatic models (e.g., Aschwanden et al. 1999b). Since the kink-mode oscillations are produced by a standing Alfvén wave with a phase speed of $v_A = B/\sqrt{4\pi m_p n_e}$, the density n_e affects the Alfvénic speed and thus the kink-mode period. Since the standard calculations assume a constant density $n_e(s)$ along an oscillating loop, the question arises whether the gravitational stratification $n_e(h) \propto \exp\left(-h/\lambda_T\right)$ with scale height λ_T affects the kink mode period or the damping rate.

Including gravitational stratification in the propagation of slow MHD waves was found to increase the damping length significantly (DeMoortel & Hood 2004) and to reduce the wave damping time by $\approx 10\% - 20\%$ (Mendoza-Briceno et al. 2004), which has also been verified by hydrodynamic simulations (Selwa et al. 2006; Gruszecki & Murawski 2008). Including gravitational stratification in a fluxtube implies a loss of symmetry, so that the normal (kink and sausage) modes are not decoupled anymore. The presence of gravity modifies also the oscillatory frequencies, the lower cutoff frequency, the fundamental to harmonic frequency ratio, and enables a coupling between surface and body modes, but the effects are small in general (McEwan & Diaz 2007; Safari, Nasiri, & Sobouti 2007; Donnelly, Diaz, & Roberts 2007; Dymova & Ruderman 2007; Karami & Asvar 2007; Taroyan & Erdélyi 2008). Exact solutions for standing kink modes of a longitudinally stratified loops were recently calculated by Dadashi et al. (2008). The combination of gravitational stratification and geometric (magnetic) field line divergence introduces an even stronger density inhomogeneity along the loop that needs to be taken into account in coronal seismology (Verth & Erdélyi 2008; Verth, Erdélyi, & Jess 2008). In particular, the gravitational density stratification causes a deviation of the fundamental to harmonic ratio P_2/P_1 from the exact value of 2 (Andries et al. 2005; McEwan et al. 2006, 2008; Dymova & Ruderman 2005, 2006), so in a reverse way, the measurement of this harmonic ratio can be used as a diagnostic of the true density scale height, which is not necessarily identical to the hydrostatic scale height (Van Doorsselaere et al. 2007). The density scale height in an oscillating loop affects also the damping rate by wave leakage, especially the scale height near the footpoints (Cally 2003).

4.3 Effects of the Hydrodynamic Time Evolution

A tacit assumption made in almost all theoretical models of MHD loop oscillations is the stationarity of density and temperature, which requires a hydrostatic equilibrium.

In order to have such a hydrostatic equilibrium, a detailed energy balance between the heating rates $E_H(s,t)$ along the loop and the conductive $E_C(s,t)$ and radiative loss rates $E_R(s,t)$ needs to be supported over an infinte time interval. Since we know from flares down to microflares and nanoflares that heating processes in the solar corona are episodic and impulsive, producing postflare loop systems that make up the bulk of an active region, the theoretical assumption of a hydrostatic equilibrium seems to be at odds with the observations. Part of the wide consensus on quasi-stationary coronal loops may come from low-resolution observations, which merge the millions of dynamic loop threads into a macroscopic entity that exhibits much less variability due to the large statistics of the loop ensemble. Recent studies with TRACE, which allows to track loop threads down to the instrumental resolution of $\lesssim 1''$, however, have demonstrated that virtually all coronal loops are first impulsively heated to soft X-ray temperatures and cool then down to EUV temperatures, with a systematic delay from hotter (284 Å) to cooler EUV filters (195 Å, 171 Å) that is consistent with radiative cooling (Winebarger, Warren, & Seaton 2003; Winebarger & Warren 2005). This leads us to a non-equilibrium scenario where an impulsive heating phase with increasing conductive loss dominates the evolution of a loop in the beginning (when it is observable in soft X-rays), while the heating stops at some point and the loop is subject to radiative cooling later on (when it is observable in EUV). Let us consider the consequences of this scenario for the detection and modeling of kink-mode oscillations.

During the cooling phase we can approximate the temperature evolution with an exponentially decaying function over some temperature range,

$$T_e(t) = T_0 \quad \exp\left[\frac{-(t-t_0)}{\tau_{cool}}\right] , \tag{19}$$

where the temperature cooling time τ_{cool} is generally dominated by the radiative cooling time τ_{rad} when observed in EUV,

$$\tau_{rad}(n_0, T_0) = \frac{9}{5} \frac{k_B T_0^{5/3}}{n_0 \Lambda_0} \tag{20}$$

where $\Lambda_0 \approx 10^{-17.73}$ erg cm^3 s^{-1} is the radiative loss rate at EUV temperatures ($T \approx 1.0$ MK). For typical loops the radiation time is of the order $\tau_{rad} \approx 10^3$ s, while the conductive cooling time would be more than two orders of magnitude longer than the radiative cooling time (e.g., see Table 3 of Aschwanden et al. 1999a).

For the evolution of the density $n(t)$ during the cooling phase we can use the *Jakimiec (powerlaw) relation* $T \propto n^a$, for which a powerlaw slope of $a \approx 2$ was found in many earlier hydrodynamic simulations (e.g., Jakimiec et al. 1992). The density evolution can thus explicitly be expressed as a function of the temperature evolution $T(t)$ (given in Eq. 19),

$$n_e(t) = n_0 \left(\frac{T(t)}{T_0}\right)^{1/2} \approx n_0 \ \exp\left[\frac{-(t-t_0)}{2\tau_{cool}}\right] . \tag{21}$$

For instance, let us consider observations in the TRACE 171 Å filter, which has a peak sensitivity at $T_0 \approx 0.95$ MK. Since the temperature response function $R_{171}(T)$ has a width of $\Delta T \approx \pm 0.15$ MK, we expect that a cooling loop appears to be visible when the temperature drops below $T \lesssim 1.1$ MK, peaks with a maximum brightness when the temperature reaches $T \approx 0.95$ MK, and fades out when the temperature drops below

$T \lesssim 0.80$ MK. Since the temperature cooling time is controlled by the radiative cooling time ($\tau_{cool} \approx \tau_{rad}$), we expect a lifetime of the loop in the 171 Å filter that amounts approximately to the radiative cooling time (of the order of $\tau_{rad} \approx 10^3$ s).

The evolution of the emission measure in the 171 Å filter is then expected for a loop with a width of w according to Eq. (21),

$$EM(t) = \int n_e^2(t)dz \approx n_e^2(t)w \ , \tag{22}$$

and the resulting flux evolution is

$$F_{171}(t) = \int EM(T[t])R_{171}(T_e)\ dT \approx n_0^2 w\ \exp\left(\frac{-(t-t_0)}{\tau_{cool}}\right) R_{171}(T[t]) \ . \tag{23}$$

Fitting the flux evolution profile to the observed flux of each loop we obtain the time t_0 when a loop cools through the peak temperature T_0 of the filter, the loop density $n_0 = n_e(t = t_0)$ at this time, the loop width w, and the cooling time τ_{cool}. The lifetime of a loop in the 171 Å filter increases with larger radiative cooling times, which is the case for lower loop densities.

For a practical example we apply this hydrodynamic model to loop oscillations observed with TRACE during the 2001-Apr-15, 22:00 UT, flare, which is described in more detail in Aschwanden & Terradas (2008). An image of the postflare arcade containing the oscillating loops is shown in Fig. 15 (top panel), while the brightness variations due to transverse kink-mode oscillations are shown in Fig. 15 (bottom panel) as a time-slice plot in perpendicular direction to the loops. The oscillatory tracks of individual loops clearly exhibit significant brightness variations as a function of time, which proves that the oscillatory loops do not have a constant density and temperature as a function of time, and thus are not in equilibrium. The brightness time profiles $I(t)$ of 8 individual loops are extracted in Fig. 16, which all show hump-like peaks above the background. This is exactly expected for a loop that cools through a TRACE passband. We can fit the expected time evolution from Eq. (23) (shown as hatched time profiles in Fig. 16) and overlay them with the actually observed time profiles (fluctuating light curves in Fig. 16). The fits yield loop densities of $n_=(1.4 \pm 0.6) \times 10^9$ cm^{-3}, loop widths of $w = 2.0 \pm 2.6$ Mm, and e-folding cooling times of $\tau_{cool} = 17 \pm 7$ min, when they cool through the peak temperature $T = 0.95$ MK of the 171 Å band. From this we conclude that oscillations of a single loop can not be detected longer than ≈10-20 min in one single filter, and thus appropriate light curve modeling is necessary to disentangle the subsequent oscillation phases of multiple near-cospatial loops.

When we analyze the time periods P and damping times τ_{damp} of a loop it is therefore imperative to restrict it to the detection time of the dominant loop at a given location, otherwise we obtain contaminations from secondary loops with different time periods, oscillation phases, and damping times. An unintended concatenation of two subsequent oscillations could introduce a much longer damping time than a single loop owns, which may invalidate the interpretation and discrimination of different physical damping mechanisms (e.g., resonant absorption vs. phase mixing). Contaminated oscillation period measurements can also corrupt the derivation of the coronal magnetic field strength and coronal shear viscosity (e.g., Nakariakov et al. 1999; Nakariakov & Ofman 2001; Nakariakov & Verwichte et al. 2005).

These results have implications from the theoretical point of view also. Since the cooling time is only three times the period of the fast kink mode, the assumption of

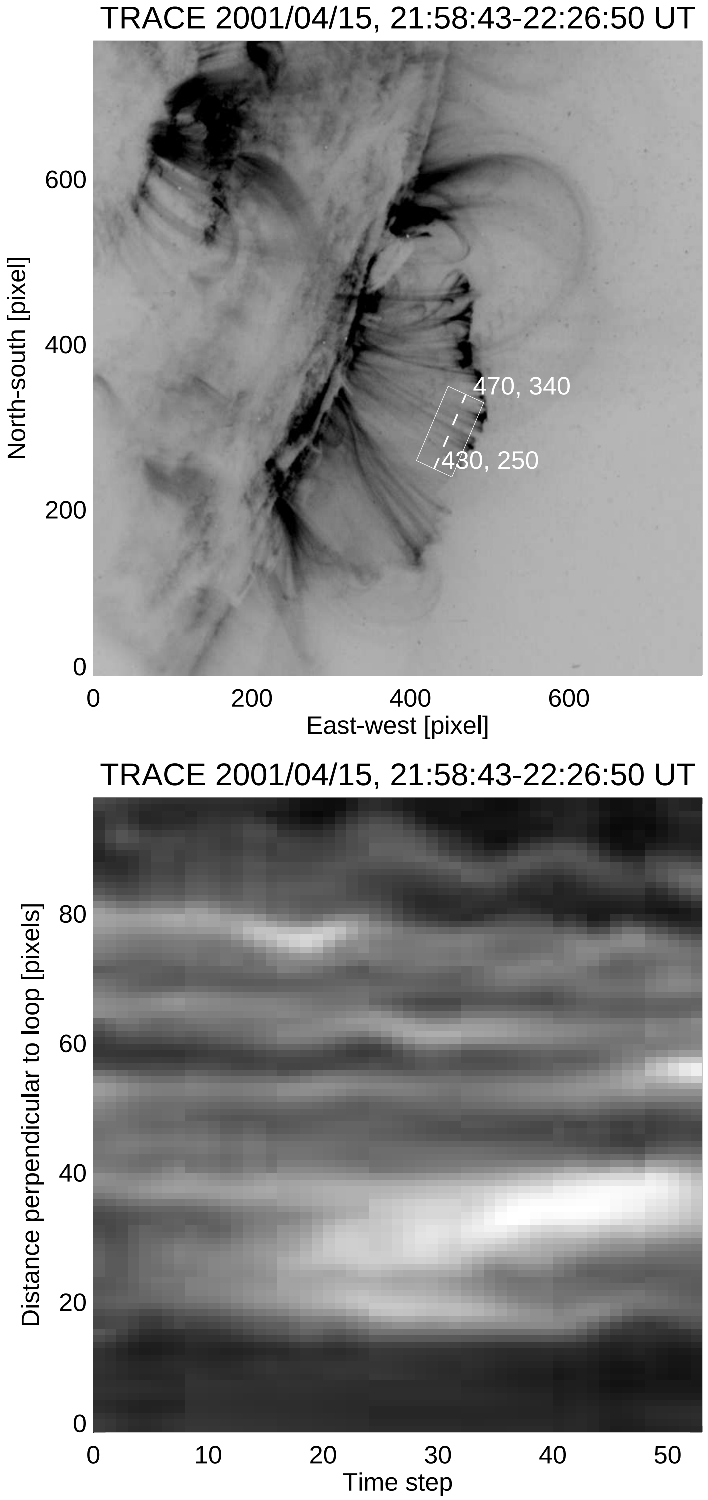

Fig. 15 *Top:* A TRACE image of postflare arcade recorded on 2001 Apr 15, 21:58:43 UT, in the 171 Å wavelength is shown. The postflare arcade exhibits swaying loop oscillations with kink-mode amplitudes transverse to the loop apexes, like a *"harmonica motion"*. *Bottom:* A time-slice from the box in the top image is extracted and shows the oscillatory motion of 8 adjacent loops. Note the brightness variations in each oscillating loop track.

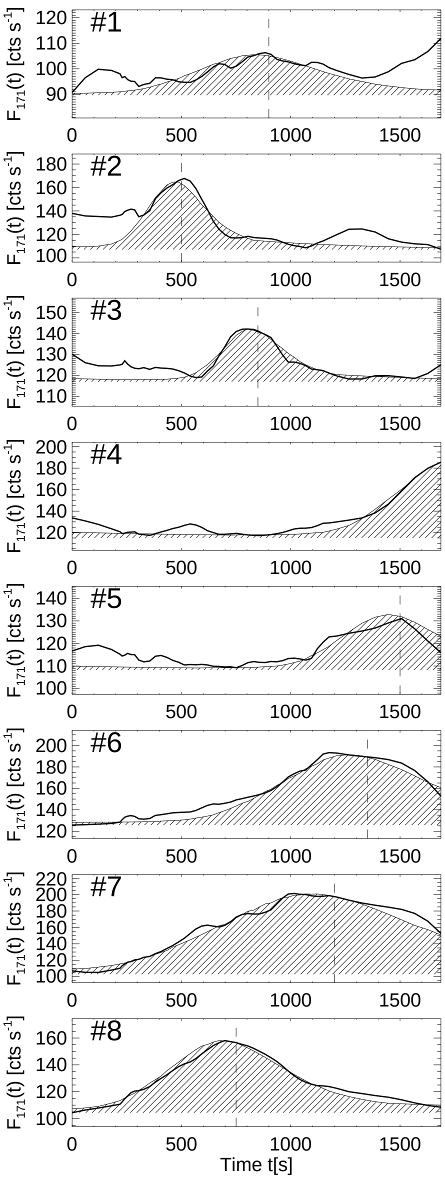

Fig. 16 The flux intensity $F_{171}(t)$ is shown for the loop centroid of the 8 oscillating loops observed at 171 Å wavelengths (thick solid line), as shown in Fig. 15. An evolutionary model of loop cooling is fitted to the main hump of the time profile (thin solid line with hatched area). The peak times t_0 are indicated with a dashed line. The best fit indicates radiative cooling times in the order of $\tau_{rad} \approx 10^3$ s.

magnetohydrostatic equilibrium used in most of the magnetohydrodynamic (MHD) models (see for example, Spruit 1982, Edwin & Roberts 1983, and Cally 1986), is clearly not justified, at least for the kink oscillations studied here. Also, the kink-mode period is expected not to be constant during cooling, but rather to decrease with time because of the density dependence, i.e. $P_{kink} = (2L/v_A)([1 + (\rho_e/\rho_0)]/2)^{1/2}$ (with L the loop half length, v_A the Alfvén velocity, and ρ_e and ρ_0 the external and internal mass densities). Thus, a proper MHD study of the kink mode for these loops should include the density and temperature changes due to the cooling process.

Proper hydrodynamic modeling of coronal loops with sufficient high spatial resolution is now possible with *Hinode/EIS* and *XRT* observations, which provide adequate temperature coverage in both EUV and soft X-rays. First Hinode observations of coronal oscillations revealed slow (acoustic) waves and fast (kink-mode) oscillations (Erdélyi & Taroyan 2008; Taroyan & Bradshaw 2008), as well as more erratic intensity oscillations associated with episodic heating (Kariyappa & Varghese 2008). The *Hinode/EIS* spectrometer provides Dopplershift measurements that allow us to model hydrodynamic flows in loops (Erdélyi & Taroyan 2008; Taroyan & Bradshaw 2008) or to perform acoustic seismology of coronal loops, using power spectra of Dopplershift time series (Taroyan et al. 2007). The *Hinode/SOT* (*Solar Optical Telescope*) moreover provides optical measurements of propagating transverse waves in loop threads, which were found to have Alfvénic speeds of $\gtrsim 1000$ km s^{-1} (Ofman & Wang 2008), which occur in loops with field-aligned subsonic flows of $v \approx 100$ km s^{-1}. The influence of such siphon flows on waves and oscillation periods in coronal loops is still little explored, but first hydrodynamic simulations show that subsonic flows do not alter MHD periods significantly, but increase the wave attenuation (Gruszecki et al. 2007). Steady chromospheric upflows can also maintain constant temperatures and densities in the loops, so that the often assumed stationarity of physical loop parameters is not such a bad assumption after all in such cases.

5 Conclusions

We find ourselves at the verge from a two-dimensional (2D) into a three-dimensional (3D) world. So far we observed the Sun with 2D images from a single spacecraft (in EUV and soft X-ray wavelengths), while we obtain now stereoscopic image pairs taken at small and large spacecraft separation angles from the STEREO twin spacecraft *Ahead* and *Behind*. For the first time we have true 3D information available, which has fundamental consequences for the data analysis and theoretical modeling of solar phenomena. In this study we explore new methods for the 3D reconstruction of coronal loops and extend them also into the forth dimension, the time domain, since coronal oscillations cannot be detected without observing their temporal evolution.

Here we explore two 3D reconstruction techniques: (1) the curvature maximization method, and (2) the stereoscopic triangulation method. The first method is applied most suitably to TRACE images, while the second method can only be performed with STEREO data. Why do we need two different methods? Although the stereoscopic triangulation method seems to be the more powerful and more accurate one, STEREO/EUVI has the two disadvantages of poorer spatial resolution ($3.2''$for EUVI vs. $1.0''$for TRACE) and short-time availability (with small-angle $\alpha \lesssim 45^\circ$ stereosocpy feasible only during the year 2007, because of the advancing spacecraft orbits). Furthermore, no large flares and CMEs occurred in 2007, and thus we have only a very limited sample of flare-induced loop oscillation observations where stereoscopy can be applied. On the other side, TRACE is superior for high-accuracy loop tracing thanks to its higher spatial resolution, which helps enormously to isolate and measure the positions of an oscillating loop within the confusion limit caused by other time-variable phenomena in the background corona along the observer's line-of-sight.

What are our first experiences with these new 3D reconstruction methods? The curvature maximization method attempts to de-project the 2D coordinates of a loop by the additional assumption of maximum curvature in 3D space, which is a genuine property of force-free magnetic fields, believed to be applicable in most parts of the solar corona (except in current sheets, reconnection regions, and in the chromosphere). Although we analyzed only one single loop with this method so far, which was located at disk center and was observed edge-on to the loop plane, this particular view reveals clearest the nonplanarity of a loop, while another view perpendicular to the loop plane would show the most circular perspective of the loop, and thus the curvature maximization method is the most efficient strategy for the reconstruction of the unseen circular perspective along the line-of-sight direction. The second loop we analyzed from EUVI data was located at the limb, with an orientation of the loop plane tilted by some 30° with respect to the line-of-sight, exhibiting a strongly elliptical shape. The curvature maximization method is not able to reveal the nonplanar shape of the loop for this particular viewpoint, but the stereoscopic triangulation method revealed a pronounced S-shape (in 2D projection) that corresponds to a helical geometry (in 3D space). This novel measurement has some unexpected consequences for theoretical modeling of kink-mode oscillations, which previously were assumed to be either horizontally or vertically polarized. The helical 3D shape possibly executes oscillations in a torsional mode, which moves us from linearly to circularly polarized kink-mode oscillations. Moreover, the helical loop shape introduces also some coupling between transverse (linearly polarized) and torsional modes, which has significant consequences for theoretical models of the damping rates. Therefore, these new results of the 3D geometry and motion of oscillating loops conjure a whole new array of theoretical models that have to be streamlined with the observed 3D motion of oscillating loops.

Also new developments in the study of the hydrodynamics of coronal loops cause some rethinking of theoretical models on MHD waves and oscillations. While previous models tacitly assumed a hydrostatic equilibrium for oscillating loops, new observations clearly demonstrate the non-equilibrium state of coronal loops seen in EUV wavelengths. Oscillating loops observed in EUV are likely to exhibit a decreasing temperature and density evolution when they cool through the EUV filters. The detectable lifetime of a loop in a narrowband EUV filter is inferred to be of order 10-20 minutes, after which the loop is invisible in the same EUV filter. This implies that no long time-series with more than $\approx 3-6$ kink-mode periods can be observed coherently, and special care has to be applied that the oscillations of near-cospatial loops are not erroneously concatenated, which would produce flawed time profiles with phase jumps, period changes, and over-estimated damping times.

In summary, both the 3D reconstruction as well as the hydrodynamic aspects require a more complicated modeling process, but on the other side we obtain more physical information on any oscillating loop system, which may lead to revolutionary conclusions. One big mystery, in particular, is the physical damping mechanism of loop oscillations, which is likely to see progress once the exponential decay times can be measured more reliably with proper geometric and hydrodynamic modeling.

Acknowledgements This work was partially supported by the NASA contract NAS5-38099 of the TRACE mission, and by NASA STEREO under NRL contract N00173-02-C-2035. The STEREO/ SECCHI data used here are produced by an international consortium of the Naval Research Laboratory (USA), Lockheed Martin Solar and Astrophysics Lab (USA), NASA Goddard Space Flight Center (USA), Rutherford Appleton Laboratory (UK), University of Birmingham (UK), Max-Planck-Institut für Sonnensystemforschung (Germany), Centre Spatiale de Liège (Belgium), Institut d'Optique Théorique et Applique (France), Institute d'Astrophysique Spatiale (France). The USA institutions were funded by NASA; the UK institutions by the Science & Technology Facility Council (which used to be the Particle Physics and Astronomy Research Council, PPARC); the German institutions by Deutsches Zentrum für Luft- und Raumfahrt e.V. (DLR); the Belgian institutions by Belgian Science Policy Office; the French institutions by Centre National d'Etudes Spatiales (CNES), and the Centre National de la Recherche Scientifique (CNRS). The NRL effort was also supported by the USAF Space Test Program and the Office of Naval Research.

References

Alissandrakis, C.E., Gontikakis, C., & Dara, H.C. 2008, Solar Phys.252, 73.

Andries, J., Arregui, I., & Goossens, M. 2005, ApJ 624, L57.

Arregui, I., Terradas, J., Oliver, R., & Ballester, J.L. 2007, A&A 466, 1145.

Aschwanden, M.J., Newmark, J.S., Delaboudiniere, J.P., Neupert, W.M., Klimchuk, J.A., Gary, G.A., Portier-Fornazzi, F., and Zucker, A. 1999a, ApJ 515, 842.

Aschwanden, M.J., Fletcher, L., Schrijver, C., & Alexander, D. 1999b, ApJ 520, 880.

Aschwanden, M.J., Nightingale, R.W., & Alexander 2000, ApJ 541, 1059.

Aschwanden, M.J., DePontieu, B., Schrijver, C.J., & Title, A. 2002, Solar Phys.206, 99.

Aschwanden, M.J., Nightingale, R.W., Andries, J., Goossens, M., & Van Doorsselaere, T. 2003, ApJ 598, 1375.

Aschwanden, M.J. 2004 (1st Edition; 2005 paperback), *Physics of the Solar Corona - An Introduction*, Praxis Publishing Ltd., Chichester UK, and Springer, New York.

Aschwanden, M.J., Nakariakov, V.M., & Melnikov, V.F. 2004, ApJ 600, 458.

Aschwanden, M.J. & Nightingale, R.W., 2005, ApJ 633, 499. 56, 577.

Aschwanden, M.J., Nightingale, R.W., & Boerner, P. 2007, ApJ 656, 577.

Aschwanden, M.J. & Terradas, J. 2008, ApJ 686, L127.

Aschwanden, M.J., Wuelser, J.P., Nitta, N.V., & Lemen,J. 2008a, ApJ 679, 827.

Aschwanden, M.J., Nitta, N.V., Wuelser, J.P., & Lemen,J. 2008b, ApJ 680, 1477.

Aschwanden, M.J., Wuelser, J.P., Nitta, N.V., & Lemen,J. 2009, Solar Phys.(subm).

Bewsher, D., Harrison, R.A., & Brown, D.S. 2008, A&A 478, 897.

Cally, P. 1986, Solar Phys.103, 277.

Cally, P. 2003, Solar Phys.217, 95.

Carter, B.K. & Erdélyi, R. 2008, A&A 481, 239.

Cooper, F.C., Nakariakov, V.M., & Tsiklauri, D. 2003, A&A 397, 765.

Dadashi, N., Safari, H., Nasiri, S., & Sobouti, Y. 2008, preprint arXiv:0802.1322

DeMoortel, I. & Hood, A.W. 2004, A&A 415, 705.

DeMoortel, I., & Brady, C.S. 2007, ApJ 664, 1210.

DeRosa, M.L., Schrijver, C.J., Barnes, G., Leka, K.D., Lites, B.W., Aschwanden, M.J., Amari, T., Canou, A., McTiernan, J.M., Regnier, S., Thalmann, J., Valori, G., Wheatland, M.S., Wiegelmann, T., Cheung, M.C.M., Conlon, P.A., Fuhrmann, M., Inhester, B., & Tadesse,T. 2009, ApJ (in press).

Diaz, A.J. 2006, A&A 456, 737.

Diaz, A.J., Donnelly, G.R., & Roberts, B. 2007, AA 476, 359.

Donnelly, G.R., Diaz, A.J., & Roberts, B. 2007, A&A 471, 999.

Dymova, M.V. & Ruderman, M.S. 2005, Solar Phys.229, 79.

Dymova, M.V. & Ruderman, M.S. 2006, A&A 459, 241.

Dymova, M.V. & Ruderman, M.S. 2007, A&A 463, 759.

Edwin, P.M. & Roberts, B. 1982, Solar Phys.76, 239.

Edwin, P.M. & Roberts, B. 1983, Solar Phys.88, 179.

Erdélyi,R. 2003, in "Turbulence, Waves, and Instabilities in the Solar Plasma", NATO Advanced Research Workshops, 16-20 Sept 2002, Budapest, Hungary, (eds. R. von Fay-Siebenburgen, K. Petrovay, B. Roberts, and M.J. Aschwanden).

Erdélyi,R. & Taroyan, Y. 2008, A&A 489, L49.

Gissot, S. & Hochedez, J.-F. 2008, Stat. Meth. 5/4, 340.

Goossens, M. 1991, *Magnetohydrodynamic waves and wave heating in nonuniform plasmas*, in E.R.Priest and A.W.Hood (eds.): *Advances in Solar System Magnetohydrodynamics*, Cambridge: Cambridge University Press, p.137.

Goossens, M., Andries, J., & Aschwanden, M.J. 2002, AA 394, L39.

Gruszecki, M., Murawski, K., Selwa,M. & Ofman, L. 2006, A&A 460, 887.

Gruszecki, M., Murawski, K., Solanki, S.K., & Ofman, L. 2007, A&A 469, 1117.

Gruszecki, M., Murawski, K., & McLaughlin, J.A. 2008, A&A 489, 413.

Gruszecki, M., & Murawski, K. 2008, A&A 487, 717.

Gruszecki, M., Murawski, K., & Ofman, L. 2008, A&A 488, 757.

Hollweg, J.V. 1990, Geophys. Res. 95, 2319.

Howard, R.A. & 45 co-authors 2008, SSRv 136, 67.

Inhester, B. 2006, *ArXiv Astrophysics e-prints*, arXiv:astro-ph/0612649.

Jakimiec, J., Sylwester, B., Sylwester, J., Serio, S., Peres, G., & Reale, F. 1992, A&A 253, 269.

Karami, K., & Asvar, A. 2007, MNRAS 381, 97.

Kariyappa, R. & Varghese, B.A. 2008, A&A 485, 289.

Klimchuk, J.A. 2000, Solar Phys.193, 53.

Klimchuk, J.A., Antiochos, S.K., & Norton, D. 2000, ApJ 542, 504.

Luna, M., Terradas, J., Oliver, R., & Ballester, J.L. 2006, A&A 457, 1071.

Luna, M., Terradas, J., Oliver, R., & Ballester, J.L. 2008, ApJ 676, 717.

McEwan, M.P., Donnelly, G.R., Diaz, A.J., & Roberts, B. 2006, A&A 460, 893.

McEwan, M.P. & Diaz, A.J. 2007, Solar Phys.246, 243.

McEwan, M.P., Diaz, A.J., & Roberts, B. 2008, A&A 481, 819.

McKenzie, D.E. 1997, PASP 109, 739.

Mendoza-Briceno, C.A., Erdélyi, R., & Sigalotti, L. Di. G. 2004, ApJ 605, 493.

Murawski, K., Selwa, M., & Rossmanith, J.A. 2005, Solar Phys.231, 87.

Nakariakov, V.M., Ofman, L., DeLuca, E., Roberts, B., & Davila, J.M. 1999, Science 285, 862.

Nakariakov, V.M. & Ofman, L. 2001, A&A 372, L53.

Nakariakov, V.M., Melnikov, V.F., & Reznikova, V.E. 2003, A&A 412, L7.

Nakariakov, V.M. & Verwichte, E. 2005, Living Reviews in Solar Physics 2, 3.

Nakariakov, V.M. & King, D.B. 2007, Solar Phys.241, 397.

Nakariakov, V.M., Aschwanden, M.J., & Van Doorsselaere, T. 2009, A&A, (subm.)

Nitta,N., VanDriel-Gestelyi,L., & Harra-Murnion,L,K. 1999, Solar Phys.189, 181.

Ofman, L. & Aschwanden, M.J. 2002, ApJ 576, L153.

Ofman, L. 2007, ApJ 655, 1134.

Ofman, L. & Wang, T.J. 2008, A&A 482, L9.

Ogrodowczyk, R. & Murawski, K. 2007, A&A 461, 1133.

O'Shea, E., Srivastava, A.K., Doyle,J.G., & Banerjee, D. 2007, A&A 473, L13.

Pascoe, D.J., Nakariakov, V.M., & Arber, T.D. 2007a, A&A 461, 1149.

Pascoe, D.J., Nakariakov, V.M., & Arber, T.D. 2007b, Solar Phys.246, 165.

Poedts, S. 2002, in *Proc. SOLMAG: Magnetic Coupling of the Solar Atmosphere Euroconference and IAU Colloq. 188*, ESA SP-505 (ed. H. Sawaya-Lacoste), Santorini, p. 273.

Priest, E.R. 1982, *Solar Magnetohydrodynamics*, Geophysics and Astrophysics Monographs Volume 21, D. Reidel Publishing Company, Dordrecht, Netherlands.

Roberts, B. 1981a, Solar Phys.69, 27.

Roberts, B. 1981b, Solar Phys.69, 39.

Roberts, B. & Nakariakov, V.M. 2003, in *"Turbulence, Waves and Instabilities in the Solar Plasma"*, NATO Science Series, Vol. 124, p. 167 (eds. Erdélyi, R., Petrovay, K., Roberts, B., & Aschwanden, M.J.), Kluwer Academic Publishers: Dordrecht.

Ruderman, M.S. & Roberts, B. 2002, ApJ 577, 475.

Ruderman, M.S. 2007, Solar Phys.246, 119.

Ruderman, M.S., Verth, G., & Erdélyi, R. 2008, ApJ 686, 694.

Safari, H., Nasiri, S., & Sobouti, Y. 2007, A&A 470, 1111.

Sandman, A., Aschwanden, M.J., DeRosa, M., Wuelser, J.P., & Alexander,D., 2009, Solar Phys.(subm.).

Schrijver, C.J., Aschwanden, M.J., & Title, A.M. 2002, Solar Phys.206, 69.

Selwa, M., Murawski, K., Solanki, S.K., Wang, T.J., & Toth, G. 2005, A&A 440, 385.

Selwa, M., Solanki, S.K., Murawski, K., Wang, T.J., & Shumlak, U. 2006, A&A 454, 663.

Selwa, M., Ofman, L., & Murawski, K. 2007, ApJ 668, L83.

Selwa, M., Solanki, S.K., Murawski, K., Wang, T.J., & Shumlak, U. A&A 454, 653.

Spruit, H.C. 1982, Solar Phys.75, 3.

Sych, R.A. & Nakariakov, V.M. 2008, Solar Phys.248, 395.

Taroyan, Y., Erdélyi, R., Doyle, J.G., & Bradshaw, S.J. 2007, A&A 462, 331.

Taroyan, Y. & Erdélyi, R. 2008, Solar Phys.251, 523.

Taroyan, Y. & Bradshaw, S. 2008, A&A 481, 247.

Terradas, J., Oliver, R., & Ballester, J.L. 2006, ApJ 650, L91.

Terradas, J., Arregui, I., Oliver, R., Ballester, J.L., Andries, J., & Goossens, M. 2008, ApJ 679, 1611.

Tomczyk, S., McIntosh, S.W., Keil, S.L., Judge, P.G., Schad, T., Seeley, D.H., & Edmonston, J. 2007, Nature 317, 1192.

Van Doorsselaere, T., Debosscher, A., Andries, J., & Poedts, S. 2004a, A&A 424, 1065.

Van Doorsselaere, T., Andries, J., Poedts, S., & Goossens, M. 2004b, ApJ 606, 1223.

Van Doorsselaere, T., Nakariakov, V.M., & Verwichte, E. 2007, A&A 473, 959.

Van Doorsselaere, T., Nakariakov, V.M., & Verwichte, E. 2008, ApJ 676, L73.

Verth, G. & Erdélyi, R. 2008, A&A 486, 1015.

Verth, G., Erdélyi, R., & Jess, D.B. 2008, ApJ 687, L45.

Verwichte, E., Nakariakov, V.M., Ofman, L., & DeLuca, E.E. 2004, Solar Phys.223, 77.

Verwichte, E., VanDoorsselaere, T., Aschwanden, M.J., Foullon, C., & Nakariakov, V.M. 2009, ApJ (subm).

Wang, T.J. & Solanki, S.K. 2004, A&A 421, L33.

Wang, T.J., Solanki, S.K., & Selwa, M. 2008, A&A 489, 1307.

Winebarger, A.R., Warren, H.P., & Seaton, D.B. 2003, ApJ 593, 1164.
Winebarger, A.R. & Warren, H.P. 2005, ApJ 626, 543.
Wuelser, J.P. & 33 co-authors 2004, Proc. SPIE 5171, 111.
Zaqarashvili, T.V. 2003, A&A 399, L15.